

THESIS FOR THE DEGREE OF DOCTOR OF PHILOSOPHY  
IN NATURAL SCIENCE

---

**Microcrystallization in lipidic cubic phase  
and serial crystallography studies of  
cytochrome *c* oxidase**

---

Cecilia Safari



UNIVERSITY OF  
GOTHENBURG

University of Gothenburg  
Department of Chemistry and Molecular Biology  
Gothenburg, Sweden, 2019

Thesis for the degree of Doctor of Philosophy in Natural Science

**Microcrystallization in lipidic cubic phase and serial crystallography studies of cytochrome *c* oxidase**

Cecilia Safari

Cover: Microcrystals of *ba*<sub>3</sub>-type cytochrome *c* oxidase in lipidic cubic phase

Copyright © 2019 by Cecilia Safari

ISBN 978-91-7833-678-4 (Print)

ISBN 978-91-7833-679-1 (PDF)

Available online at <http://handle.net/2077/62148>

Department of Chemistry and Molecular Biology  
Division of Biochemistry and Structural Biology  
University of Gothenburg  
SE-405 30, Göteborg, Sweden

Printed by BrandFactory AB  
Göteborg, Sweden, 2019

*Till Pierre*



## ABSTRACT

Life in all living organisms depend on chemical processes performed by proteins, which are molecular machineries encoded in the DNA. Cytochrome *c* oxidase (CcO) is a membrane protein essential for cellular respiration, a process in which chemical energy enters the electron transport chain in the form of electrons and is transformed to ATP via a proton gradient. In the active site of CcO a redox-reaction takes place, where oxygen that we breathe is reduced to two water molecules at the same time as protons are pumped over the membrane.

This thesis focuses on structural investigations performed by serial crystallography (SX) of CcO in lipidic cubic phase (LCP). The advances of bright X-ray sources in the form of X-ray Free Electron Lasers with short pulse durations and 4:th generation synchrotrons have evolved the structural biology field in the sense that high-quality data can be collected at room temperature with minimal X-ray induced radiation damage. These advancements enable the capturing of structural intermediates of proteins in a time-resolved manner.

Well-diffracting microcrystals are of essence in serial crystallography experiments, and the study of membrane proteins in lipidic cubic phase has proven to be favorable compared to detergent-based crystallization. This thesis focuses on developing procedures to produce microcrystals in LCP, and its use in studies of *ba*<sub>3</sub>-type CcO from *Thermus thermophilus* as well as reaction centre from *Blastochloris viridis*. The room-temperature structure of *ba*<sub>3</sub>-type CcO is determined in both the resting oxidized state and the reduced CO-bound state. The resting state structure reveals the active site ligand as a single oxygen species, and in comparisons to previously published structures of CcO we show structural differences between *ba*<sub>3</sub>-type CcO and bovine *aa*<sub>3</sub>-type CcO upon CO-binding. The work presented in this thesis provides the groundwork for future time-resolved CO-photolysis experiments of *ba*<sub>3</sub>-type CcO by the pump-probe approach, which may reveal more about the structural mechanisms that explain proton pumping in CcO.



## LIST OF PAPERS

- Paper I** R. Andersson, C. Safari, R. Dods, E. Nango, R. Tanaka, A. Yamashita, T. Nakane, K. Tono, Y. Joti, P. Bath, E. Dunevall, R. Bosman, O. Nureki, S. Iwata, R. Neutze & G. Branden. “Serial femtosecond crystallography structure of cytochrome *c* oxidase at room temperature” *Scientific Reports* 7, 4518 (2017) doi: 10.1038/s41598-017-04817-z
- Paper II** R. Andersson ‡, C. Safari ‡, P. Bath, R. Bosman, A. Shilova, P. Dahl, S. Ghosh, A. Dunge, R. Kjeldsen-Jensen, J. Nan, R. L. Shoeman, M. Kloos, R. B. Doak, U. Mueller, R. Neutze and G. Branden. “Well-based crystallization of lipidic cubic phase microcrystals for serial X-ray crystallography experiments” *Acta Cryst.* (2019). D75, 937-946  
doi: 10.1107/S2059798319012695  
‡ These authors contributed equally
- Paper III** P. Båth, P. Börjesson, C. Safari, R. Dods, R. Andersson, R. Bosman, C. Wickstrand, T. Björg Ulfarsdottir, P. Dahl, M.-J. García-Bonete, J.-B. Linse, G. Ortolani, E. Dunevall, S. Ghosh, E. Nango, S. Owada, R. Tanaka, T. Nakane, A. Yamashita, K. Tono, Y. Joti, T. Tanaka, T. Arima, O. Nureki, S. Iwata, G. Brändén, R. Neutze. “Lipidic cubic phase serial femtosecond crystallography structure of a photosynthetic reaction centre” *Manuscript* (2019)
- Paper IV** C. Safari, R. Andersson, S. Ghosh, J. Johannesson, P. Båth, R. Bosman, P. Dahl, E. Nango, R. Tanaka, E. Dunevall, P. Börjesson, O. Uwangué, D. Zoric, G. Hammarin, M. Panman, E. Svensson, G. Ortolani, T. Tanaka, T. Tosha, H. Takeda, H. Naitow, T. Arima, A. Yamashita, M. Sugahara, T. Nakane, O. Nureki, S. Iwata, R. Neutze & G. Brändén “Room-temperature structure of CO-bound *ba*<sub>3</sub>-type cytochrome *c* oxidase reveals mechanistic differences between A-type and B-type enzymes” *Manuscript* (2019)

## Related papers

- Paper V** R. Dods, P. Båth, D. Arnlund, K. R. Beyerlein, G. Nelson, M. Liang, R. Harimoorthy, P. Berntsen, E. Malmerberg, L. Johansson, R. Andersson, R. Bosman, S. Carbajo, Elin Claesson, Chelsie E. Conrad, P. Dahl, G. Hammarin, M. S. Hunter, C. Li, S. Lisova, D. Milathianaki, J. Robinson, C. Safari, A. Sharma, G. Williams, C. Wickstrand, O. Yefanov, J. Davidsson, D. P. DePonte, A. Barty, G. Brändén, R. Neutze "From macrocrystals to microcrystals: a strategy for membrane protein serial crystallography" *Structure*. (2017) Sep 5;25(9):1461-1468.e2, doi: 10.1016/j.str.2017.07.002

## CONTRIBUTION

### **Paper I**

I cultivated cells, purified protein and was involved in producing figures for the manuscript.

### **Paper II**

I cultivated cells, purified protein and developed the crystallization protocol. I collected data at two experiments, and took part in preparing the manuscript.

### **Paper III**

I was involved in developing the crystallization method. I participated in the experiment and did sample preparation.

### **Paper IV**

I purified protein, developed the crystallization protocol and produced the crystals. I led the practical work at three experiments, processed the data and prepared the manuscript.

# TABLE OF CONTENTS

<b>I. INTRODUCTION</b>	<b>1</b>
<b>1. CELLULAR METABOLISM</b>	<b>2</b>
1.1 CELLULAR RESPIRATION	2
1.2 OXIDATIVE PHOSPHORYLATION AND CHEMIOSMOSIS	3
<b>2. CYTOCHROME C OXIDASE</b>	<b>5</b>
2.1 HEME-COPPER OXIDASES	5
2.2 REACTION CYCLE OF O <sub>2</sub> REDUCTION	7
2.3 PROTON TRANSFER PATHWAYS	8
2.4 ELECTRON TRANSFER	9
2.5 PROTON PUMPING AND THE PROTON LOADING SITE	10
2.6 LIGAND CHANNEL	11
<b>3. SCOPE OF THIS THESIS</b>	<b>13</b>
<b>II. METHODOLOGY</b>	<b>15</b>
<b>4. PROTEIN PRODUCTION AND CHARACTERIZATION</b>	<b>15</b>
4.1 PROTEIN EXPRESSION: GROWTH OF BA <sub>3</sub> - TYPE CcO IN <i>THERMUS THERMOPHILUS</i>	15
4.2 PROTEIN PURIFICATION	16
4.3 ABSORPTION SPECTROSCOPY OF BA <sub>3</sub> -TYPE CcO	17
<b>5. STRUCTURE DETERMINATION OF PROTEINS USING X-RAYS</b>	<b>19</b>
5.1 ESSENTIALS OF PROTEIN CRYSTALLOGRAPHY	19
5.2 MEMBRANE PROTEIN CRYSTALLIZATION WITH FOCUS ON THE LCP METHOD	20
5.3 FROM SYNCHROTRONS TO X-RAY FREE ELECTRON LASERS	23
5.4 SERIAL CRYSTALLOGRAPHY WITH FOCUS ON SFX	24
5.5 DATA PROCESSING WITH CRYSTFEL AND STRUCTURAL REFINEMENT	28
<b>III. RESULTS AND DISCUSSION</b>	<b>33</b>
<b>6. MICROCRYSTALLIZATION IN LCP (PAPER I, II, III, IV)</b>	<b>33</b>
6.1 SCREENING AND PRODUCING MICROCRYSTALS FOR SFX-EXPERIMENTS	33
6.2 AN ENCLOSED SYSTEM FOR CO-BOUND CcO IN MICROCRYSTALS	38
6.3 SUMMARY	41
<b>7. ROOM-TEMPERATURE SFX-STRUCTURE OF BA<sub>3</sub> CcO IN THE RESTING STATE (PAPER I)</b>	<b>42</b>

7.1	ROOM TEMPERATURE DATA COLLECTION OF $BA_3$ -TYPE $CcO$ IN THE RESTING STATE	42
7.2	SFX STRUCTURE OF $BA_3$ -TYPE $CcO$ FREE FROM RADIATION DAMAGE: COMPARISON TO A CRYOGENIC LCP STRUCTURE	42
7.3	STRUCTURAL DIFFERENCES AT THE ACTIVE SITE AND THE PROTON LOADING SITE	44
7.4	SUMMARY	46
<b>8.</b>	<b>CO-COMPLEXED <math>BA_3</math>-TYPE <math>CcO</math> DEDUCED BY SERIAL FEMTOSECOND CRYSTALLOGRAPHY (PAPER IV)</b>	<b>48</b>
8.1	SFX-DATA COLLECTION, PROCESSING AND STRUCTURAL REFINEMENT	48
8.2	SFX STRUCTURE OF REDUCED CO-BOUND $BA_3$ -TYPE $CcO$ AT ROOM TEMPERATURE	49
8.3	STRUCTURAL COMPARISON OF THE CO-BOUND, OXIDIZED AND REDUCED STATES OF $BA_3$ -TYPE $CcO$	52
8.4	STRUCTURAL ALTERATIONS OF HELIX X IN $AA_3$ -TYPE $CcO$ ARE ABSENT IN $BA_3$ -TYPE $CcO$	52
8.5	SUMMARY	54
<b>9.</b>	<b>INITIAL RESULTS FROM PUMP-PROBE SFX WITH DISSOCIATION OF CO FROM THE ACTIVE SITE OF <math>BA_3</math>-TYPE <math>CcO</math></b>	<b>55</b>
9.1	PUMP-PROBE DATA COLLECTION, PROCESSING AND GENERATION OF INITIAL DIFFERENCE ELECTRON DENSITY MAPS	55
9.2	INITIAL RESULTS FROM PUMP-PROBE DATA COLLECTION	55
9.3	DISCUSSION AND FUTURE PROSPECTS	56
<b>10.</b>	<b>CONCLUSIONS AND FUTURE PERSPECTIVES</b>	<b>58</b>
<b>IV. POPULÄRVETENSKAPLIG SAMMANFATTNING</b>		<b>61</b>
<b>V. ACKNOWLEDGEMENTS</b>		<b>63</b>
<b>VI. BIBLIOGRAPHY</b>		<b>67</b>



## I. INTRODUCTION

“The circle of life” is truly a good expression for describing how all of nature’s processes are connected. About 2.3-2.5 billion years ago and before our planet was a habitable place for aerobic organisms, photosynthetic cyanobacteria in the deep seas performed photosynthesis. These bacteria breathed  $\text{CO}_2$  using water as reducing agent and harvested sunlight as energy source in order to produce sugar as storable energy and the bi-product oxygen. Photosynthesis is the process that gave rise to all oxygen on earth. Chronologically, cyanobacteria photosynthesized first and later eukaryotic green algae evolved from the same ancestor [1]. Photosynthesizing organisms contain proteins, co-factors and pigments called chlorophylls. The chlorophylls have the ability to absorb the sun’s photonic energy and are organized into light harvesting complexes, which pass the absorbed light energy further to what is called a Reaction center (RC). A special pair of chlorophylls in RC transfer the absorbed energy in the form of electrons. The electrons are used in the electron transport chain, which is a set of membrane-bound protein complexes, to create a proton gradient across the membrane. The proton gradient is used to generate adenosyl triphosphate (ATP) by what is called photophosphorylation. ATP is the chemical energy currency in all living organisms and is used by photosynthetic bacteria, algae and plants to convert  $\text{CO}_2$  and water into carbohydrates.

Life on earth requires oxygen to survive and thrive, and all cells must perform cellular respiration in order to drive their cellular processes. In opposite to photosynthetic organisms, the animal kingdom needs chemical energy in the form of carbohydrates, fats and proteins that originate from plant-based carbon sources. However, the animal kingdom needs to produce and use the same energy currency, ATP, to drive all cellular processes in order to live. ATP is produced by the process called oxidative phosphorylation and as the name implies, oxygen is needed to produce ATP. Chemical energy from food is extracted in the form of electrons, which are donated to the electron transport chain and passed to  $\text{O}_2$  as the final electron acceptor. Similar to photoautotrophs, the electron transport chain of animal- and bacterial cells produce an electrochemical proton gradient across the membrane, that is used to generate ATP. The bi-products of cellular respiration are water and carbon dioxide which is breathed out and recycled by plants in photosynthesis.

As described, elements in nature are recycled in the processes of photosynthesis and cellular respiration. This thesis will focus mainly on the last electron accepting protein in the electron transport chain of oxidative phosphorylation, called cytochrome *c* oxidase (CcO). CcO transfers electrons to O<sub>2</sub> at the same time as it pumps protons against the proton gradient, producing a potential energy that drives ATP-synthesis. The mechanism of proton pumping in CcO has been studied within the field of bioenergetics for many years, yet the proton pumping mechanism remains unclear. In this thesis, novel approaches in protein crystallography are explored for serial crystallography experiments. The methods have been applied to structural studies of the anatomy of cytochrome *c* oxidase with X-ray radiation. Hopefully, new approaches in structural biology will help us to better understand the structural-functional relationship of proton-pumping in CcO.

## **1. Cellular metabolism**

The metabolic pathways in the cell include all processes maintaining life. The pathways can be categorized into anabolic or catabolic processes, in which molecules can be synthesized or broken down, respectively. The anabolic processes are always endergonic ( $+\Delta G$ ) while catabolic processes are exergonic ( $-\Delta G$ ). Cellular respiration is a catabolic pathway where energy is released in the breakdown of nutrients to produce ATP. Breakage of the phosphate bonds in ATP releases energy that can drive endergonic cellular processes, such as protein synthesis or cell division.

### **1.1 Cellular respiration**

Digestion of macro- to micronutrients (e.g. to glucose or acetate) is the preparatory work before energy can be absorbed and metabolized by cells in order to produce ATP. The steps in aerobic cell respiration are glycolysis, pyruvate oxidation, the citric acid cycle (or Krebs cycle), electron transport and ATP-synthesis. The first three steps are localized in the cytoplasm or mitochondrial matrix, and the last two steps are membrane-integrated. Below follows the start- and end compounds in oxidative phosphorylation, without mentioning the vast number of intermediates that are part of each step.

Type of reaction:	Metabolite	
1) Glycolysis	glucose	→ Pyruvate, ATP, NADH
2) Pyruvate oxidation	pyruvate	→ Acetyl-CoA + NADH
3) Citric acid cycle	Acetyl-CoA	→ GTP, NADH, FADH <sub>2</sub>
4) Electron transport chain	NADH, FADH <sub>2</sub>	→ H <sup>+</sup> -gradient
5) ATP-synthesis by H <sup>+</sup> -gradient	H <sup>+</sup> -gradient	→ ATP

## 1.2 Oxidative phosphorylation and chemiosmosis

Peter Mitchell, the biochemist who first presented the chemiosmotic theory in the 1960's, stated that ATP-synthesis is coupled to redox reactions in cell respiration and photosynthesis via an energy-intermediate, being the electrochemical proton gradient. His postulation was not popular in the community at the time, but was awarded the Nobel Prize in 1978 [2]. The processes of electron transport, proton pumping and chemiosmosis take place across the inner mitochondrial membrane of eukaryotes and across the cytoplasmic membrane of prokaryotes. Taken together there are five membrane-integrated proteins named complex I-V, of which complex I-IV contain redox-catalyzing cofactors, see figure 1. These co-factors (flavins, coenzyme Q, heme-groups, and copper atoms) donate electrons from low-potential groups that are reducing to high-potential groups that are oxidizing. The electron transfers reactions in complex I, II and IV drive proton pumping [3]. The inner side of the membrane has a net negative charge while the exterior side has a net positive charge (referred to as the N- and P-sides respectively). Proton pumping occurs from the N- to P-side, which builds up a transmembrane energy gradient. The gradient is composed of an electric potential ( $\Delta\psi$ ) due to the created charge difference over the membrane, and a chemical potential due to the concentration- or pH-difference of H<sup>+</sup> ( $\Delta\text{pH}$ ) across the membrane. The electrochemical gradient is used by complex V as a proton-motive force, powering the flux of protons through a pore of complex V (F<sub>0</sub>ATP-synthase), which in turn drives the rotary molecular motor in the N-side of the complex (F<sub>1</sub>ATP-synthase) leading to phosphorylation of ADP to ATP. Phosphorylation of ADP to ATP is a highly endergonic process that usually goes in the opposite direction [4].

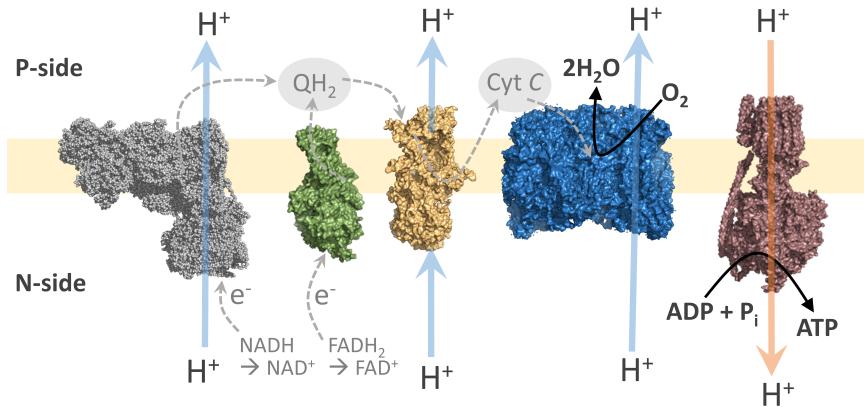


**Figure 1.** Model of mitochondrial electron transport complexes I, II, III, IV and complex V are depicted from left to right with PDB IDs 5LDW, 3ABV, 5KLV and 3WG7. Blue arrows indicate proton pumping and the red arrow proton flux. Energetic electron pairs that are bound to NADH enter the ETC via complex I (NADH dehydrogenase). These electrons traverse through complex I via redox reactions at the same time as four protons are pumped across the membrane. The electrons are passed to quinone (Q), a lipid-soluble carrier molecule. In parallel, complex II (succinate dehydrogenase) engages electrons to the ETC by succinate via FADH<sub>2</sub>, donating electrons to Q without pumping any protons. When fully reduced, quinol (QH<sub>2</sub>) transports the electrons to complex III (cytochrome *bc*<sub>1</sub> complex), which absorbs two electrons from QH<sub>2</sub> being passed one by one to water-soluble carrier molecule cytochrome *c* (CytC) located in the intermembrane space. At the same time, four protons are pumped over the membrane. CytC shuffles electrons to complex IV where the final electron acceptor is oxygen. Oxygen is reduced by four electrons to two water molecules at the same time as four protons are pumped over the membrane per oxygen molecule. The transmembrane potential energy created by the proton gradient is used by complex V (F<sub>0</sub>F<sub>1</sub>-ATP-synthase) to produce ATP.

## 2. Cytochrome c oxidase

An average adult consumes 550 L oxygen and produces almost 1 kg of carbon dioxide on a daily basis [5]. About 90% of the consumed oxygen in breathing organisms are consumed by cytochrome *c* oxidases [6]. CcOs belong to the superfamily of terminal heme-copper oxidases, in which quinol oxidases also are included [7].

### 2.1 Heme-copper oxidases

By definition, the class of heme-copper oxidases contain a low-spin heme (e.g. heme *a* or heme *b*) and the binuclear center (BNC), consisting of a heme  $a_3$  and a copper ion termed  $\text{Cu}_B$  in subunit I. These redox sites are ligated by six conserved histidines that also belong to subunit I [8]. Other conserved residues are a valine-I, important for  $\text{O}_2$ -diffusion and an arginine-I, important for proton exit (see review [9]). The heme-copper oxidases are generally divided into the A- ( $aa_3, bo_3$ ), B- ( $ba_3$ ) and C- ( $cbb_3$ )-types, and the A-types are the most studied [10]. CcOs in mitochondria, *Paracoccus denitrificans* and *Rhodobacter sphaeroides* are all  $aa_3$ -types.

The core of CcO is highly conserved in the  $aa_3$ -type CcOs consisting of subunits I, II and III. In mitochondria, these three subunits are coded in mitochondrial DNA and the remaining 10 subunits are coded in the nuclear DNA, creating a large complex of 220 kDa.  $aa_3$ -oxidases in *R. phaeooides* and *P. denitrificans* only have one subunit added to the conserved core, making them approximately half the size. CcOs of types B and C lack subunit III in the conserved core and subunit II varies some as well. The  $ba_3$ -oxidase solely possess subunits I, II and a third one denoted IIa, having a mass of 84 kDa and is depicted in figure 2.

The first complete crystallographic structure of CcO was published in 1995 of the  $aa_3$ -type in *P. denitrificans* at 2.8 Å resolution [11]. Shortly after, the first mitochondrial CcO was published at the same resolution [12]. In year 2000, the structure of  $ba_3$ -type CcO was published [13], and two years later the structure of the  $aa_3$ -type from *R. sphaeroides* [14] was solved. The structural features of the core subunits I, II and III in  $aa_3$ - and  $ba_3$ -oxidases are briefly described below.

*Subunit I* consists of twelve transmembrane helices that settle in a tilted position within the membrane. The helices are organized as assemblies forming three polar pores, containing side-chains of polar amino acids and water molecules. Two out three pores are known to be critical for proton transfer and pumping, and the third one is suggested to be used for proton pumping solely in mitochondria. Heme *a* and the BNC are buried

separately in two pore clusters and are ligated by six conserved histidines [9]. The transmembrane helices have lipidic properties while the loops that are localized on the P- and N- sides have hydrophilic amino acid residues. Mitochondrial  $aa_3$ -type CcO have a zinc ion without known catalytic function in proximity to heme  $a$ . The  $ba_3$ -type CcO harbors one additional helix apart from the twelve in  $aa_3$ -oxidase and has a low spin heme  $b$  instead of heme  $a$ .

*Subunit II* harbors the first electron-accepting site in CcO which is a dicopper site termed  $Cu_A$ .  $Cu_A$  is located in a ten-sheet beta cluster on the P-side of the membrane, easily accessible for electron donation from CytC. Further, subunit II of  $aa_3$ -oxidases have two transmembrane helices that are associated to subunit I while the  $ba_3$ -oxidase only contains one helix that connects to subunit I [13]. Localized between subunit I and subunit II is a buried magnesium ion unique for the  $aa_3$ -type CcO, considered to be important for re-localizing waters produced at the BNC [15] and also important for proton pumping[16].

*Subunit III* is unique for  $aa_3$ -type CcO; it is highly hydrophobic and has no functional redox-role. Yet it increases the catalytic lifetime of CcO by stabilizing subunit I and by upholding rapid proton flow [17].

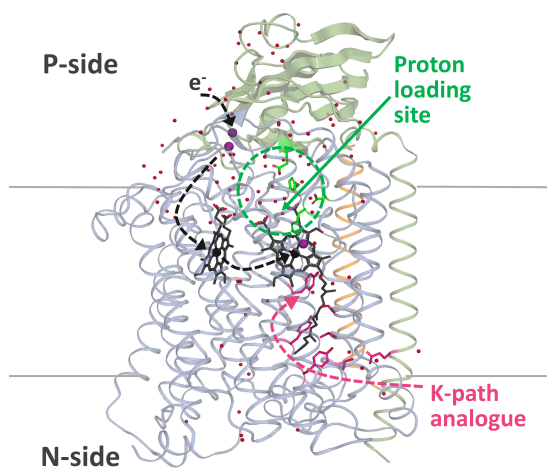


**Figure 2.** The structure of  $ba_3$ -type CcO. The black arrows indicate the electron transfer path from  $Cu_A \rightarrow$  heme  $b \rightarrow Cu_B$  and heme  $a_3$ . The dashed green line highlights the proton loading site and the pink dashed line shows the K-path analogue for substrate protons and protons to be pumped.

## 2.2 Reaction cycle of O<sub>2</sub> reduction

In order to simplify the discussion, the catalytic cycle of A-type CcOs is described in this section; the stoichiometry and kinetics vary between classes of CcO. The elements that participate in redox chemistry are heme *a*<sub>3</sub> and Cu<sub>B</sub> (the BNC), heme *a*, Cu<sub>A</sub> and a conserved tyrosine that is covalently bonded to a histidine, linked to Cu<sub>B</sub> [18]. The catalytic cycle involves a reductive phase and an oxidative phase as seen in figure 3 and both phases involve electron transfer and proton pumping. The oxidative phase comprises O<sub>2</sub>-binding and oxidation of BNC [Cu<sup>+</sup> → Cu<sup>2+</sup>] and [Fe<sup>2+</sup> → Fe<sup>4+</sup>] and the reductive phase involves reduction of BNC and the release of 2H<sub>2</sub>O before next O<sub>2</sub> binds [19].

The BNC must be reduced by two electrons (redox-states Fe-*a*<sub>3</sub><sup>2+</sup> and Cu<sub>B</sub><sup>+</sup>) in order for O<sub>2</sub> to bind. This state is denoted as **R** and as soon as O<sub>2</sub> binds to heme *a*<sub>3</sub>, state **A** is formed. From state **A** follows the **P<sub>R</sub>** or **P<sub>M</sub>**-state, in which the O-O bond is cleaved and each oxygen atom ligates to Fe<sub>a3</sub> and Cu<sub>B</sub> respectively. In the case when CcO is fully reduced (four electron reduction) by artificial reductants, heme *a*, Cu<sup>+</sup> and Fe<sub>a3</sub><sup>2+</sup> donate one electron each to O<sub>2</sub>, forming **P<sub>R</sub>**. In the other case being when CcO is naturally reduced, electrons are donated from Cu<sup>+</sup>, Fe<sub>a3</sub><sup>2+</sup> and the hydroxyl of the redox active tyrosine (Y-OH) forming the **P<sub>M</sub>**-state. The reaction via **P<sub>M</sub>** takes longer time since a more demanding rearrangement of the active site takes place. Y-OH also donates a proton in both P-intermediates. The steps after **P<sub>M/R</sub>** are as following: **P<sub>M/R</sub>** → **F** → **O<sub>H</sub>** → **E** → **R**. In each of these steps, electron transfer is coupled to substrate proton delivery to the BNC. Each transfer further equals to one pumped proton across the membrane and a total of 4 H<sup>+</sup><sub>p</sub> [20]. The resting state of oxidized CcO (i.e. not during catalytic turnover) is **O** for *aa*<sub>3</sub>-type CcO with Fe-*a*<sub>3</sub><sup>3+</sup> and Cu<sub>B</sub><sup>2</sup> as redox-states. In paper I, we show that the active site ligand of *ba*<sub>3</sub>-type CcO is a single oxygen species such as a water or a hydroxide ion instead of a peroxide, as proposed in previous structures (paper I).

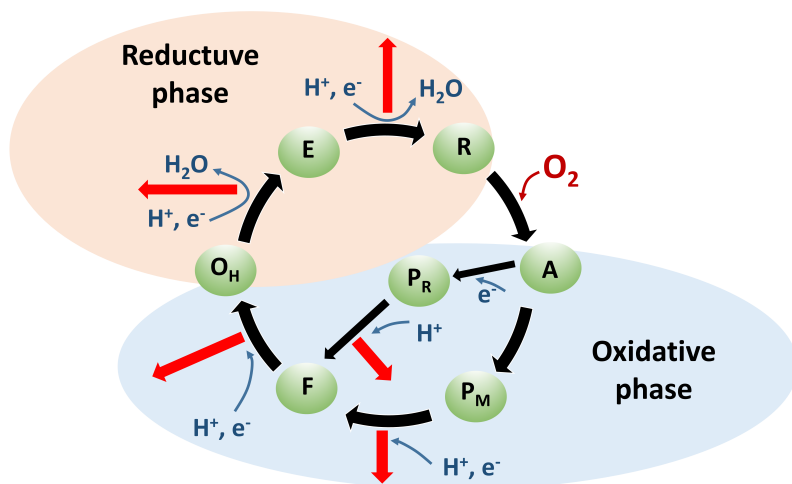


**Figure 3.** The catalytic cycle of CcO (*aa*<sub>3</sub>-type). The oxidative phase runs from the R-state → O<sub>H</sub>-state (blue circle), while the reductive phase runs from O<sub>H</sub> → R (pink circle). A red arrow indicates one pumped proton. The route from A → F can go through either the P<sub>M</sub>- or P<sub>R</sub> intermediate. P<sub>M</sub> is the natural route with two electrons reducing the BNC and P<sub>R</sub> is the artificial route with four electron reduction of the BNC. This figure is adapted from [20].

### 2.3 Proton transfer pathways

The catalytic site in CcO is deeply embedded in subunit I, thus proton delivery here must be performed efficiently. Mutational and crystallographic studies has helped to identify proton channels that can lead protons to the BNC for catalytic reaction and pump protons from the N- to P-side, or perform both processes. In the bacterial *aa*<sub>3</sub>-type CcO, two proton channels have been identified denoted as the D- and K-paths [18] which are both located in subunit I. It has been hypothesized that an additional proton pathway exists in the mitochondrial *aa*<sub>3</sub>-type CcO named the H-path [21]. The shared factor for all the proton paths is hydrogen-bonding networks, established by polar amino acids and fixed- or mobile water molecules.

**The D-path** The D-path starts with an aspartate residue in subunit I, which is exposed to the N-side. The aspartate is the proton-uptake site, and the proton path is hydrophilic half-way through the membrane and contain a glutamate residue in the middle, of importance for proton pumping in bacterial *aa*<sub>3</sub>-type CcOs. The other half of the path is hydrophobic and leads to the BNC. It is suggested that mobile water molecules and side-

chain shifts enable the proton highway in between [10]. The D-path in bacterial *aa*<sub>3</sub>-type CcOs is used to transfer two substrate protons to the BNC and all four protons to be pumped across the membrane, counted per O<sub>2</sub>. The mitochondrial *aa*<sub>3</sub>-type CcO is suggested to use the D-pathway solely for proton delivery to the BNC by two substrate protons per O<sub>2</sub> molecule, but there is no full consensus. The B- and C-type CcOs lack any proton translocating function in the corresponding region, which could be a reason for their less efficient proton pumping kinetics [10].

**The K-pathway:** The K-pathway (K-path) has its name from a conserved lysine, which is necessary for its functionality [22]. The proton uptake site is suggested to be at a glutamate residue belonging to subunit II; it is however not as polar as the D-path and is only functional in the A-type CcOs. The K-path solely delivers two substrate protons to the BNC [18] per O<sub>2</sub> molecule.

**The K-path analogue:** The pores that correspond to the D- and K-paths are not functionally conserved in the *ba*<sub>3</sub>-type CcO, which solely has one proton conducting channel called the K-pathway analogue (K-path analogue), depicted in figure 2. The K-path analogue transports both substrate protons to the BNC and protons to be pumped across the membrane. It overlaps in space with the K-path, and includes the cross-linked tyrosine close to the BNC [9]. In the *ba*<sub>3</sub>-type CcO, approximately two protons are pumped per O<sub>2</sub> molecule via the K-path analogue and all four substrate protons are translocated through this pathway [23].

**The H-pathway:** There is a controversy about the role of the H-pathway (H-path); a complete path exists in the bovine *aa*<sub>3</sub>-type CcO while the polar residues seen here are not fully conserved in neither yeast- nor bacterial *aa*<sub>3</sub>-type CcOs [24]. Mutations in the H-path and computations show lack of function of this route in yeast and bacteria. It is suggested that the H-path either works as a dielectric well [25-27] or that it leads all four protons to be pumped across the membrane. The H-path consists of a water channel and a hydrogen bond network leading almost all the way from the N- to P-side. In contrast, the D- and K-paths lead from the N-side to the BNC [28].

## 2.4 Electron transfer

Electrons are introduced to CcO when CytC docks into the surface of subunit II and forms a brief complex. CytC donates one electron at a time to Cu<sub>A</sub>, consisting of two copper atoms that are ~2.5 Å apart. The electron is then passed from Cu<sub>A</sub> to heme *a* (or heme *b* in *ba*<sub>3</sub>-type CcO) located ~12 Å away, which is ~1/3 into the membrane. The electron is further passed from heme *a* to the BNC by first reaching Cu<sub>B</sub>, before it reduces

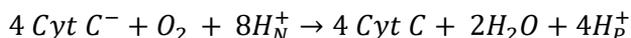
heme  $a_3$  and reaches  $O_2$  as the last electron acceptor [10]. Long-distance transfer of electrons in protein matrixes such as CcO or the ETC occur by electron tunneling. This process is a quantum mechanical phenomenon, in which the protein matrix works as the carrier medium by lowering the tunneling energy between redox-active metal clusters that contain e.g. iron-, copper-, or magnesium ions. Because of this mechanism electrons in cells can travel up to 30 Å and the tunneling time can be down on 10 fs [29].

## 2.5 Proton pumping and the proton loading site

Peter Mitchell successfully deduced that the energetic coupling between redox-reactions and ATP-synthesis is an electrochemical proton gradient. His theorem was not sufficient to explain the pumping mechanism of CcO and today we know that complexes I, III and IV perform pumping by different mechanisms that are not equivalent to other enzymes [30]. The pumping mechanism of complex I was recently formulated and involves redox-coupled antiporter-like subunits pumping protons through *indirect coupling*, meaning that proton pumping and redox reactions are spatially separated processes that can be coupled by conformational changes. Complex III and IV pump protons by *direct coupling*, where e.g. a cofactor facilitate the redox-reaction and proton uptake within the protein [30]. In complex III, the carrier molecule Q cycles electrons and protons via the Q-cycle as suggested by Mitchell [31].

In  $aa_3$ -type CcO, one electron is transferred from the P-side and one proton from the N-side to the BNC. Both of the charges move in a vectorial fashion, corresponding to one charge equivalent transferred from the N- to the P-side and building up a charge separated state. CcO creates a charge separated state *and* pumps one excess proton over the membrane per electron transfer. This can be viewed as an event where two positive charges translocate across the membrane per electron transfer and is depicted in figure 4. M. Wikström provided the energy calculations that supported the proton-pump theorem of CcO showing that 75% of the free energy generated by electron transfer from CytC to  $O_2$ , was conserved by CcO, instead of 36% as Mitchell initially proposed [32].

The reaction scheme in  $aa_3$ -type CcO is as follows:



In order for proton pumping to occur in a redox-coupled fashion, the free energy created by the redox reaction must be conserved and not lost as heat. A proposed pump scheme is that CcO picks up the proton to be

pumped before the substrate proton is transferred to the catalytic site for water formation [33]. The concept of a proton loading site (PLS) has been coined, being the site within CcO where the protons to be pumped are stored before pumped to the P-side. Conceptually, it is important that the PLS has interchanging access to the two sides of the membrane, otherwise a short circuit could form leading to spontaneous proton flux from the P- to the N-side [34]. Conformational changes, or different protonation states, could switch the access of the PLS to either the N-side ( $H^+$ -loading) or to the P-side ( $H^+$ -pumping). Proton loading and pumping could occur by the following affinity changes at the PLS: in the loading phase, a high  $pK_a$  at the PLS enables proton-binding from the N-side and  $pK_a^{PLS} > pK_a^{N-side}$  while in the pumping phase,  $pK_a^{PLS} < pK_a^{P-side}$  which enables proton release to the P-side.

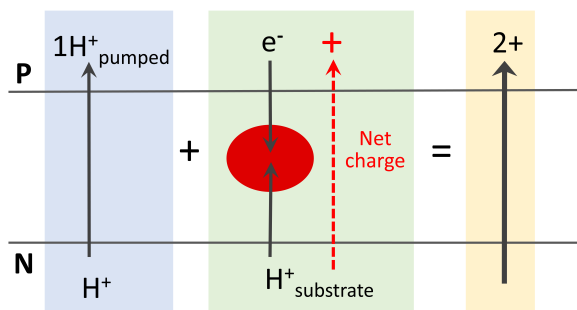


**Figure 4.** Vectorial charge translocation in A-type CcO. In total, two net positive charges are transferred to the P-side per electron transfer.

## 2.6 Ligand channel

The route for oxygen diffusion through CcO has been studied with a combination of crystallographic studies and mutations close to the BNC, involving Xenon-pressurized crystals and MD-simulations [14, 35]. These studies show that a hydrophobic oxygen channel starts in the membrane region of subunit I with two entry points that merge in proximity to the BNC. Oxygen delivery to the catalytic site seems to differ between CcOs; in *aa*<sub>3</sub>-type CcOs a narrowing of the channel is caused by large amino acid residues (tryptophan or phenylalanine), blocking oxygen passage. No studies have been able to explain the mechanism for O<sub>2</sub> passage through the constriction point, and it is proposed that some conformational change is needed to allow for oxygen passage [35]. The oxygen channel is located in the same region in *ba*<sub>3</sub>-type CcO, but is broader around a conserved and

important region with a valine. Blockage of the valine-region has profound effects in O<sub>2</sub>-binding rates that are not seen in *aa*<sub>3</sub>-type CcOs [36]. This supports the notion that oxygen has a more direct access to the BNC in *ba*<sub>3</sub>-type CcO while some conformational activation must occur for O<sub>2</sub>-transport in the *aa*<sub>3</sub>-type CcO.

### 3. Scope of this thesis

The aim of this thesis has been to elucidate the structure of a membrane protein termed *ba*<sub>3</sub>-type cytochrome *c* oxidase and to develop novel procedures for microcrystallization of proteins in lipidic cubic phase. The structures of CcO and two other membrane proteins were determined by producing microcrystals used for serial crystallography experiments at a synchrotron and at an X-ray free electron laser source.

The first aim of the project was to produce microcrystals of *ba*<sub>3</sub>-type CcO in lipidic cubic phase. We managed to produce microcrystals by modifying a previously published condition, which yielded the first room-temperature structure of a cytochrome *c* oxidase, free from the effects of radiation damage, determined at 2.3 Å resolution (**paper I**). In paper I, we propose that a single oxygen species is ligated in the active site of *ba*<sub>3</sub>-type CcO in the oxidized resting state and highlight differences between *ba*<sub>3</sub>- and *aa*<sub>3</sub>-type CcOs. Subsequently, we polished the crystallization used in paper I and developed an effective crystallization protocol adapted for screening and producing large scales of microcrystals in lipidic cubic phase, which is convenient for monitoring the crystallization process. The presented work resulted in the well-based method for microcrystallization of proteins in lipidic cubic phase, published in **paper II**. The well-based method was used to produce a new non-toxic crystallization condition for *ba*<sub>3</sub>-type CcO and to find novel crystallization conditions for a bacterial reaction centre and sensory rhodopsin II. The crystals of *ba*<sub>3</sub>-type CcO were also used for the first user serial crystallography experiment performed at MAX IV Laboratory. The well-based method and a previously reported seeding technique were used to produce microcrystals of a photosynthetic reaction center that contained the important co-factor Ubiquinone-2, diffracting to a resolution of 2.3 Å (**paper III**). A procedure was developed to produce reduced carbon monoxide bound microcrystals of *ba*<sub>3</sub>-type CcO anaerobically, and to deliver them into the X-ray chamber at the SPring-8 Angstrom Compact free electron Laser without exposure to oxygen. The procedure is presented in **paper IV**, together with the structure of the reduced CO-bound SFX-structure of *ba*<sub>3</sub>-type CcO, determined at room-temperature. We compare our CO-bound SFX-structure to bovine CO-bound *aa*<sub>3</sub>-type CcOs and highlight the structural differences in the inter-heme region upon CO-binding to the active site. We propose a difference in the structural response that is linked to ligand binding between *ba*<sub>3</sub>- and *aa*<sub>3</sub>-type CcOs, presumed to influence proton pumping.



## II. METHODOLOGY

### 4. Protein production and characterization

Structural studies of proteins with X-ray crystallography often demand several milligrams of good-quality, stable and pure protein for screening and production of protein crystals. Membrane proteins are generally harder to produce than soluble proteins; the production- and purification yields are lower, and the proteins are much more instable when solubilized with detergents from their native membranes. Protein engineering methods have been very useful to solve the mentioned problems [37].

#### 4.1 Protein expression: growth of *ba*<sub>3</sub>- type CcO in *Thermus thermophilus*

The process of acquiring a satisfactory protein sample could be simply by expressing the protein in its native host organism, given that natural protein production yields are high. In recombinant protein expression, the target gene can be inserted into a DNA-vector that transfects a host cell, producing higher amounts of protein than the native host. Expression of the target gene can be manipulated by altering cell growth conditions. Examples of problems that could be encountered are poor yield, formation of inclusion bodies, inactivation of protein, poor posttranslational modifications involving misfolding or glycosylation.

The *ba*<sub>3</sub>-type CcO in this work was produced in the extremophile *Thermus Thermophilus*, a gram-negative bacteria having its native environment in hot springs. *T. thermophiles* of strain HB8 is a facultative anaerobic bacterium that optimally grows at 60-75 °C. At these temperatures, oxygen solubility in water is very low. At 70 °C O<sub>2</sub>-solubility is 60% less compared to solubility at 25 °C. *T. thermophilus* expresses two terminal CcOs: the *caa*<sub>3</sub>-type and the *ba*<sub>3</sub>-type. The *caa*<sub>3</sub>-type has low oxygen affinity while the *ba*<sub>3</sub>-type has high affinity for oxygen. The *ba*<sub>3</sub>-type CcO is expressed under anaerobic or low-oxygen conditions while the *aa*<sub>3</sub>-type is continuously expressed [38].

We produced recombinant *ba*<sub>3</sub>-type CcO having a 6-polyhistidine-tag in the N-terminal of subunit I and a selection marker for Kanamycin in the transfected vector, as described in [39]. The cell growth and protein yields were optimized from a previous cell culturing protocol to obtain the optimum ratio of protein per grams of cells [40]. Cultures of *T.*

*thermophilus* were grown in 3-liter or 5-liter flasks (non-baffled), filled with 73% growth media. The flasks were covered with aluminum foil and sealed with layers of parafilm. The cultures were incubated at 110 rpm for 3-4 days.

## 4.2 Protein purification

Extraction and purification of membrane-bound proteins involve several steps, and the general procedures are cell disruption, membrane extraction, protein solubilization and protein purification by chromatographic methods. Cell lysis can be performed by chemical, enzymatic or mechanical methods. The latter involves e.g. sonication, bead grinders or high-pressure homogenization that produces shear forces on the cell sample when altering from low-to-high pressure. All methods break the cell walls and disrupt the cell membrane. Sonication was used to break *T. thermophilus* cells, where burst cycles of 60 seconds were followed by 60 seconds of cooling. The cell lysate was kept on ice during sonication and protease inhibitor was added to the cell suspension. The cell debris was separated from the membrane by centrifugation; dense cell compartments were removed by preparative centrifugation and cell membranes were collected with ultracentrifugation. Collected membrane was homogenized and the membrane proteins were solubilized with detergents. Proteins must in general be reconstituted into a hydrophobic membrane-mimicking environment when they are removed from the native phospholipidic bilayer into solution. Reconstitution can be done by detergents micelles, bicelles, lipids, liposomes, nanodiscs or even polymers. We used the detergent Triton-X, a non-ionic mild detergent, to solubilize *ba*<sub>3</sub>-type CcO. Detergents have a hydrophilic part (a head) and a hydrophobic part (a tail), which form micelles above a certain concentration and temperature. The hydrophobic tails point inwards (away from the solution) in a spherical constellation. When adding detergents, lipid-lipid and lipid-protein interactions in the cell membrane are broken and micelles are formed around the protein that shield them from the aqueous phase [41].

After solubilization, the target protein need to be isolated from the protein cocktail and its chemical- and physical properties are used for purification in liquid chromatography. The protein cocktail is passed through resins that separate the target protein according to binding affinity, charge or protein mass. In the case of *ba*<sub>3</sub>-type CcO, three purification steps were used; immobilized affinity chromatography (IMAC), ion-exchange chromatography (IEC) and size-exclusion (SEC) chromatography. The IMAC contained a matrix with nickel, binding to histidines in the protein such as the six-polyhistidine tag in the recombinant *ba*<sub>3</sub>-type CcO. The

protein was eluted from the column by competitive binding by imidazole. Subsequently, IEC separated the protein with respect to the isoelectric point (pI) of the protein and the buffer pH. Here, DEAE (diethylaminoethanol) resin was used which is an anion exchange column. The isoelectric point of *ba*<sub>3</sub>-type CcO being 7.3 [42] and a buffer condition of pH 7.6 allowed protein binding to the positive matrix. The protein was eluted with a buffer having high salt concentration. In cases when increased purity was required after the two first purification steps, SEC was performed as a last step. In SEC, the proteins pass a matrix containing gel beads with pores. Proteins with high molecular masses do not pass through the small pores and therefore elute faster than small proteins. Small proteins and molecules enter the pores of the matrix and have a longer pathway and retention time through the SEC-matrix.

### 4.3 Absorption spectroscopy of *ba*<sub>3</sub>-type CcO

Absorption spectroscopy is a method where spectral characteristics of molecules are used to identify or quantify molecules. The absorbance of molecules are wavelength dependent and correlate to the energies where their electrons can absorb, e.g. in the ultraviolet and visible range. The beam attenuation of the incident light is proportional to the absorption by the Beer-Lambert law, which can be used to calculate the concentration of the absorbing molecule.

A heme-group consist of a di- or trivalent iron in the cavity of an aromatic porphyrin ring and substituent(s). Porphyrins are naturally abundant in the form of heme-groups e.g. in hemoglobin and chlorophyll and can have different metal ions such as cobalt-, magnesium- or copper ions.

The Soret-band of heme-groups are usually located near the 400 nm-range and the Q-band around 500-600 nm. In CcO, absorption peaks change with the redox-states of the Cu<sub>A</sub> and iron ions in heme *a*, heme *b* and heme *a*<sub>3</sub> due to changed energy levels, thus Cu<sub>B</sub> does not contribute. Ligand-binding also changes the absorbance signature. Figure 5 assign the redox peaks of the dominant co-factor [43, 44]. Moreover, the surroundings of CcO such as pH, also affect the spectral features [45].

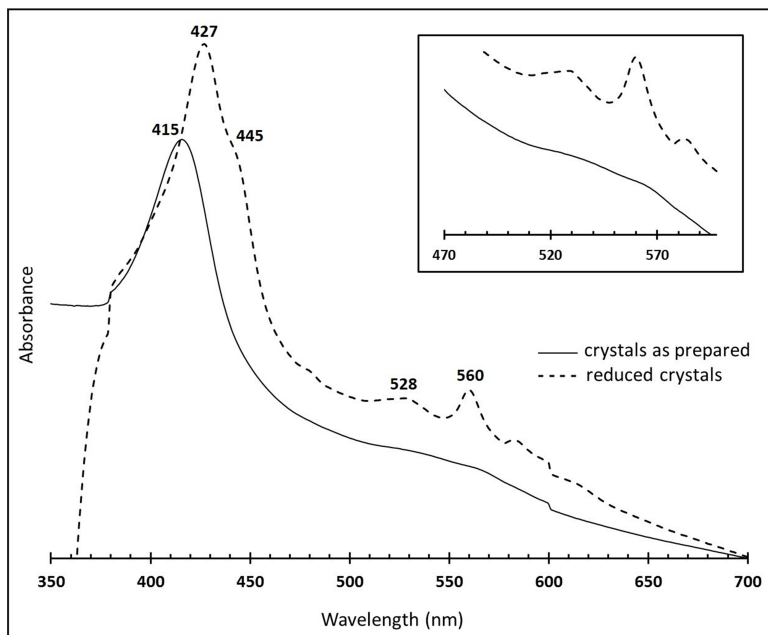


**Figure 5.** UV-Vis absorbance spectrum of  $ba_3$ -type crystals of CcO in oxidized (black line) and fully reduced (dashed line) states. Heme  $b$  contributes to the oxidized peak at 414 nm and the reduced peaks at 427, 528 and 560 nm. Heme  $a_3$  contributes to the reduced shoulder at 445 nm.

## 5. Structure determination of proteins using X-rays

Proteins are the macromolecular machineries in all living life and are constituted of the elements carbon, hydrogen, nitrogen and oxygen. In order to identify individual atoms within a protein, wavelengths must be used that correspond to the bond distances between the atoms. The length of a covalent single bond between two organic carbon atoms is approximately 1.5 Å ( $1.5 \times 10^{-10}$  m) and the distance between a hydrogen bond donor and its acceptor is somewhere around 2.4-3.5 Å. The wavelength of X-rays are in the same order of magnitude (1-100 Å), meaning they can scatter individual atoms within a protein.

### 5.1 Essentials of protein crystallography

Crystals function as amplifiers of the diffraction signal; one single crystal contains many thousands of ordered proteins that amplify the intensity of the diffracted wave when X-rays hit the crystal. The smallest repetitive entity that can be translated to build up the whole crystal is called a unit cell. The unit cell possess the full symmetric properties that are found in the crystal, more precisely the space group and Miller indices that build up the crystal lattice. The unit cell itself can comprise of many asymmetric units, which builds up the whole unit cell by symmetry operations (translation, rotation and rototranslation). X-rays penetrate most materials and can thus not be focused by objective lenses. Instead, the reflections of X-rays are used to create an image of the object in reciprocal space. The proteins within a crystal are arranged in a periodic, repetitive manner and create atomic planes. The atomic planes scatter the incoming X-rays, and if Bragg's law is satisfied, constructive interference occurs. In order for constructive interference to occur in reciprocal space the Ewald condition must be fulfilled. The reflections that are coincide with any surface point of the Ewald sphere with the radius  $r = 1/\lambda$  are produced as diffraction spots or reflections, and the crystal must be rotated a certain degree to cover all possible reflections that can be produced by the crystal lattice.

$$n \lambda = d \sin (\theta) \quad (1)$$

In Bragg's law, which is depicted in equation 1 and figure 6,  $n$  is an integer meaning that X-rays are in phase,  $\lambda$  is the wavelength of the X-rays,  $d$  is the spacing between the atomic planes and  $\theta$  is the incident and outgoing angles. The incoming X-ray has the same energy after scattering due to elastic scattering.

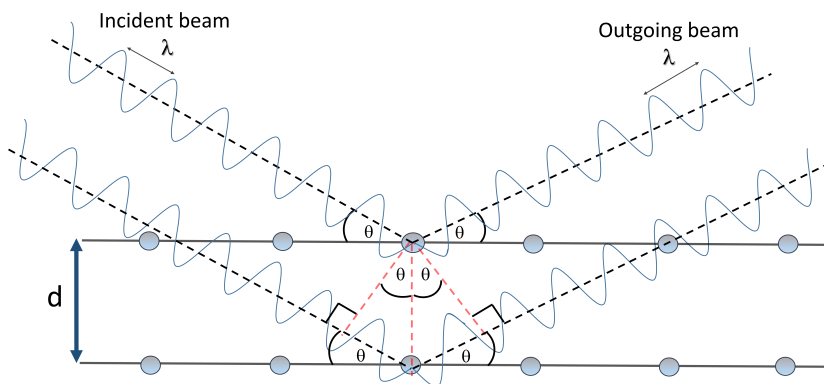


**Figure 6.** Representation of Bragg's law in a crystal, where  $d$  is the distance between atomic planes and  $\theta$  is the incident angle of the incoming X-ray of wavelength  $\lambda$ . Atoms are represented as blue spheres.

Fortunately, the image in reciprocal space can be converted to a real space image by a Fourier transformation. The reflections can be described as structure factors  $\vec{F}_{hkl}$ , with an amplitude  $F$  and a phase (directionality),  $\varphi$ . However, the conversion of reflections is not unproblematic. The amplitude can be deduced after Fourier transformation, but not the phases, and this is denoted the phase problem. There are different ways of approaching the phase problem, e.g. by using the properties of heavy metals and/or different absorption edges for atoms: single/multiple isomorphous replacement (SIR/MIR) or multiple/single-wavelength anomalous dispersion (SAD/MAD). The most commonly used method to solve the phase problem is molecular replacement (MR), where an already known protein structure serves as a template. The template structure amplitudes  $F_{\text{calc}}$  and observed structure amplitudes  $F_{\text{obs}}$  are transformed into Patterson maps.  $F_{\text{obs}}$  is compared and matched to  $F_{\text{calc}}$  by rotation and translation in the unit cell. The right superposition between  $F_{\text{obs}}$  and  $F_{\text{calc}}$  give the estimated phases from  $\varphi_{\text{calc}}$ ,  $\vec{F}_{hkl}$  comprising  $F_{\text{obs}}$  and  $\varphi_{\text{calc}}$ .

## 5.2 Membrane protein crystallization with focus on the LCP method

Protein crystallization is sometimes referred to as an art form due to the difficulty of finding right crystallization conditions. The first protein structure was solved in 1958 from crystals of myoglobin [46]. In general,

membrane proteins are harder to crystallize than soluble proteins and it took more than 20 years before the first crystal structure of the integral membrane protein reaction center was solved [47]. Membrane proteins are harder to produce in large quantities and are more difficult to keep stable in solution due to deprivation of their native lipid bilayer environment in solubilization. Adding to that, the protein population must be homogenous and have high purity [48, 49]. The advances in protein engineering and the development in crystallization strategies have made membrane protein crystallization more accessible. The two main crystallization strategies are the *in surfo* and *bilayer* methods. *In surfo* crystallization is detergent based and examples are vapor diffusion, hanging-drop, dialysis, capillary counter diffusion and micro-batch (oil-based). In the *Bilayer method* protein is constituted in a lipidic bilayer instead of detergent micelles. The bilayer method include *in meso* crystallization (lipidic cubic phase or sponge phase), bicelle crystallization or crystallization in vesicles [50].

### ***In surfo* crystallization**

Protein crystallization can be described as slow and gentle precipitation by the aid of chemical agents. The right composition and concentration of protein, detergent, lipid, precipitant, salt, buffer, pH and temperature affects protein solubility and drive the protein from an under-saturated state to supersaturation. A schematic of the solubility curve is seen in figure 7. Supersaturation is a non-equilibrium, non-ordered labile state where protein concentration is above the solubility limit. In the supersaturated state, small partially ordered assemblies or aggregates form called crystal nuclei. Free protein concentration decreases when crystal nuclei grow and a metastable equilibrium state in solid form when growth is completed [51].

### ***Crystal contacts***

Crystallization trials of membrane proteins have been rationalized with robotics and commercial screens, and there are different crystallization strategies that can be tried out. Crystal contacts form between the uncovered soluble parts of membrane proteins that are crystallized *in surfo* [49]. In bilayer-based crystallizations hydrophobic interactions mainly form crystal contacts and show superior crystal packing [52, 53]. Factors such as instability in the detergent environment, loss of structural lipids and masking of surface/polar areas important for crystal contacts could inhibit crystal formation when using detergents instead of lipids. Crystal contacts can be modified by adding stable polar domains such as antibodies [54, 55], or by embedding the protein in a lipidic environment

instead of detergent usage. Lipid environments include e.g. bicelles, lipidic cubic phase or nanodiscs. Bicelles are lipid disks that are soluble in aqueous environment, and these form when mixing a detergent or a small lipid with a long-tailed lipid. When the temperature is increased and passes the transition temperature, a non-soluble perforated lamellar phase is created. After bicelle reconstitution, proteins can be treated just as in detergent-based crystallization [56, 57]. The downside with this method is the low mesophase stability which restricts the detergents that can be used for crystallization screening [58].

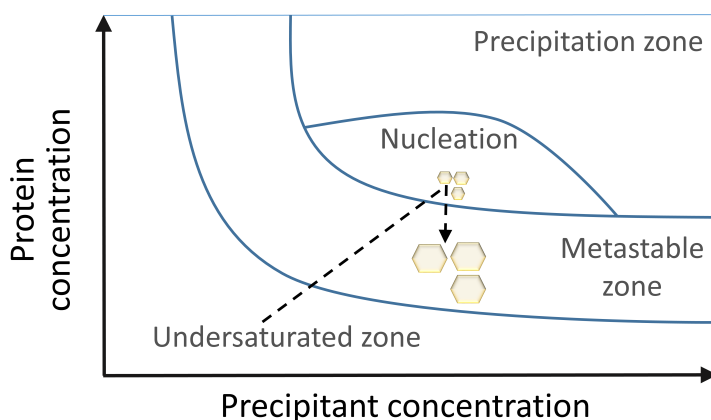


**Figure 7.** Protein solubility curve for the *in surfo* crystallization approach. Crystal nuclei form when the protein solubility is altered by the protein- and precipitant concentrations. Crystal nuclei growth lowers protein concentration and shift the solubility state to the metastable zone.

### ***LCP crystallization***

Monoacylglycerols (MAGs) are usually used for *in meso* crystallization in lipidic cubic phase. MAGs have amphiphilic properties, the most common one being monoolein (9.9 MAG) having a polar glycerol head connected to a hydrocarbon tail with an ester bond. Monoolein has been extensively used in crystallization of membrane proteins. Its usage has led to many high-resolution structures and is sometimes referred to as a “magic lipid”[59]. MAGs have distinct phase properties when heated above the transition temperature and pass different liquid crystalline states when melted. The molecules crystallize spontaneously and the crystal forms vary depending on the hydration level and temperature [59]. By adding 20-40% solvent to monoolein, the cubic phase forms having a gel-like,

high-viscosity consistency composed of three different but similar crystalline space groups. A simplified phase diagram of the monoolein-water system in the vicinity of 20 °C is shown in figure 8. The cubic phase is bicontinuous, meaning that it consists of the lipid bilayer and the aqueous phase continuously in 3D [60]. The lipid bilayer thickness and the diameter of the water channels can vary [61]. Protein in the aqueous phase freely diffuse in the plane of the bilayer of the cubic phase. When the LCP is distributed into precipitant solution, mesophase properties are transformed and phase separation occurs. The protein accumulates in one of the separated phases and give rise to nucleation sites [60]. Precipitant solution molecules (salts, PEGs) can be solvated in the water channel networks and have been shown to alter the morphology of LCP crystals [61].

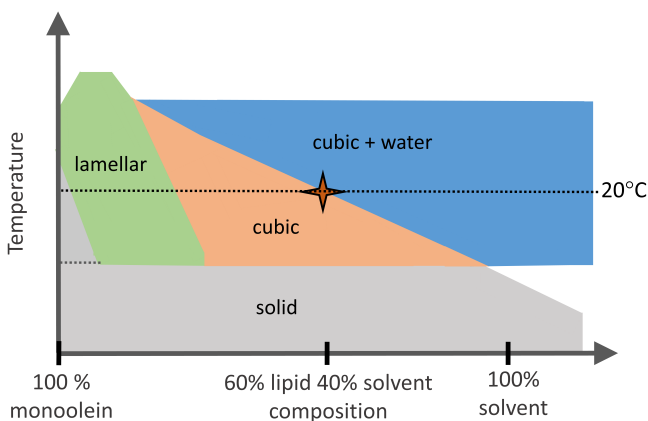


**Figure 8.** Phases of the monoolein-water system equilibrium-composition phase diagram. The cubic phase is denoted by a star and comprises 60% monoolein (9.9 MAG) and 40% solvent at 20 °C. The figure is recreated from [62].

### 5.3 From synchrotrons to X-ray free electron lasers

X-rays were discovered by Wilhelm Röntgen in 1895, and in 1912 M.V. Laue and P. Knipping confirmed the space-lattice arrangements of atoms in crystals. One of the most historically noticed events is the discovery of the DNA-structure, awarded the Nobel prize to Watson, Crick and Wilkins, and it was based on Rosalind Franklin’s X-ray crystallography studies of DNA[63].

In the 1960’s synchrotrons revolutionized the structural biology studies of biomolecules while in present time the evolution of X-ray Free-electron

lasers (XFELs) are the breakthrough. Both sources produce X-rays by accelerating charges in a magnetic field, forcing the electrons to change direction and making the electrons emit electromagnetic radiation. Synchrotrons comprise of rings containing magnets where injected electrons are accelerated and circulated. XFELs have undulator magnets leading electrons in a straight path. The main limitations of synchrotron capacity compared to XFELs are as follows:

*Brightness or brilliance:* The brightness of the X-rays are 100-million to a billion times higher in XFELs compared to synchrotrons (which can also be expressed as photons/mode). *Pulse duration/ repetition rate:* An XFEL beam consists of pulse-trains, that come in periodic bunches. As a leading example, the European XFEL produces 2700 pulses per 0.1 ms in each pulse train, each pulse being 10-100 fs in duration. The pulse duration is shorter than the span of time for chemical reactions, which opens up for the recording of “molecular movies” of chemical reactions. Also, the short pulse duration enables recording of the diffraction data before the onset of radiation damage. *Pulse quality:* Compared to synchrotron X-rays, pulses that emit from XFELs possess spatial coherence which means that the waves are in phase. In an XFEL, free electrons are generated from an electron gun and further accelerated to relativistic speeds. The electromagnetic field force the electrons to propagate in a sine-wave along the undulator magnets. When electrons interact with the electromagnetic fields, radiation is spontaneously emitted and stimulate other electrons to emit radiation in an exponential fashion. This process is called self-amplified spontaneous emission (SASE) and in final bunched electrons emit intense radiation coherently. Since electrons propagate freely, wavelength of the formed radiation can be monitored by e.g. changing acceleration energy [64].

The future of XFELs is bright – the construction of the EU-XFEL provides multiuser capabilities, only possible at synchrotrons before now. LCLS II will have a repetition rate of 1 MHz (instead of 120 Hz) when commissioned and the EU-XFEL has a repetition rate of 27 MHz, SwissFEL 100 Hz, PAL-XFEL 60 Hz and SACLA 60 Hz.

## **5.4 Serial crystallography with focus on SFX**

### ***Comparison of rotational and serial crystallography***

In rotational crystallography (RX) a crystal (usually bigger than 20x20x20  $\mu\text{m}^3$  in size [65]) is collected in a cryo-loop with a metal base that is magnetically mounted onto a goniometer. The assembly is then rotated (and translated) while the crystal is exposed to X-rays in order to collect the Bragg reflections and cover the entire symmetry of the crystal. In order

to slow down crystal damage caused by X-ray radiation, crystals are flash-frozen in liquid nitrogen prior to mounting, and a cryo-stream at near 100 K is sprayed on the crystals during data collection. The cryogenic condition can however damage the crystal lattice which is why a cryo-protectant at right concentrations is needed in the mother liquor during crystal growth. Alternatively matured crystals are soaked into a cryo-protectant (e.g. glycerol, sucrose, lipids) before cryo-freezing. Radiation damage is one of the major drawbacks in RX and is caused by the atoms ability to absorb the X-rays. X-ray absorption create ionizing photo-electrons by free radicals. These species can in turn perturb the protein structure by reducing heavy atoms and sulfur-containing side chains, breaking carboxylates to CO<sub>2</sub> and destroy other interatomic interfaces. The primary damages can lead to secondary radiation damage involving destruction of the crystal lattice. Cryo-freezing prevents X-ray induced disorder of the lattice to some extent but the high-resolution areas might not be covered if atom movements are too big [66]. Intermediate states of active site in metalloproteins are particularly sensitive to radiation damage, heme-proteins are easily reduced in a radiation dose-dependent fashion that can be avoided by SFX data collection without the usage of cryo-protectants [67].

### ***Serial crystallography***

Many of the issues encountered in RX are circumvented in the application of serial crystallography (SX), including serial synchrotron crystallography (SSX) and serial femtosecond crystallography (SFX). In 2000 it was suggested that very short exposures to X-ray pulses of high intensities (such as XFEL radiation) would enable collection of X-ray data before crystal damage, expressed as “diffraction before destruction” [68]. In SX, nano- to micrometer sized crystals < 20 μm can be used owing to the brightness and high-focus of the X-ray beams at 4:th generation synchrotrons [69] and XFELs. In SX, crystals are positioned in random orientations and collected diffraction spots are only partial reflections. When thousands of microcrystals have been shot at, their intensities can be merged to a 3D reflection list and further processed. Another advantage of SX is the more natural state of proteins in room-temperature data collection compared to cryogenic data conditions, and the possibility to study proteins by pump-probe experiments.

### ***Sample delivery systems in SX***

In serial microcrystal delivery systems, new crystals are ideally delivered to the X-ray beam after probing the previous crystal, without wasting

crystals. There are different types of injectors that can perform this, depending on the crystal media. For crystals in solution, a liquid jet can be created using a GVDN (gas-dynamic virtual nozzle) which focuses the crystals to a stream of 1-6  $\mu\text{m}$  with gas pressure at high flow rates, up to  $10 \text{ ms}^{-1}$ . This injector has the drawback of wasting the vast majority of sample since one of ten thousand crystals is probed [70]. Other types of injectors wasting less sample are high-viscosity injectors such as LCP-injectors [70]. LCP injectors are preferably used in combination with viscous carrier matrixes, not compromising diffraction properties or giving background noise [71]. Furthermore, silicon chips with micropores for crystals are used in fixed-target SFX, in which silicon chips are attached to e.g. a roadrunner goniometer [72]. Examples of other sample delivery systems are acoustic droplet ejection in which picoliters of crystals are delivered to the X-ray beam [73], or electro-kinetic injection which injects a small sample stream of crystals (in glycerol or PEG solution) under an electric field, forming a solid sample stream of  $\sim 0.17 \mu\text{l/minute}$  [74].

In papers I, III and IV the high-viscosity LCP-injector at SACLA [75] was used which is a modified version of the LCP-injector presented in [70]. This injector consists of a hydraulic stage that is HPLC-driven, a modified sample reservoir of cartridge-type that can hold 60  $\mu\text{l}$  sample instead of 20/45  $\mu\text{l}$ , and an exchangeable nozzle with an inner diameter of 75 or 100  $\mu\text{l}$ . Two teflon balls push the sample forward and seal the sample as pressure is applied from the plunger. A type of syringe injector [76] was also tried out which extruded sample directly from a packed 100- $\mu\text{l}$  Hamilton syringe through a short needle. The syringe delivery system did not deliver a stable sample jet on axis, but instead curled and adhered to the injection needle. This issue could have been caused by the lack of shear force from a co-flowing gas surrounding the sample jet, present in the other type of LCP-injector that was used [70].

Data collection was performed in a helium sample chamber [77], thus the temperature did not decompose the LCP-phase as risked *in vacuo* collection [78]. Good sample flow is extra important in time resolved experiments, and the sample flow is affected by many factors: sample pressure, nozzle diameter, sample viscosity, flow speed and gas environment being some of them.

### ***Detectors***

The demand for successful data collection in SX is single X-ray photon sensitivity and fast read-out, matching the repetition rates. The detectors are developed to maximize the measureable peak signal and the

development of these have been pushed since the advancement of hard XFEL-sources. The general principle for detectors are that X-ray photons are absorbed by the detector and create drifting charges, read-out as signals by the processing circuitry [79]. At SACLA, an adapted monolithic X-ray pixel detector has been developed with a multi-port charge-coupled device (MPCCD) [80] while Biomax at MAXIV uses an Eiger X 16M (Dectris, Switzerland) hybrid pixel X-ray detector.

### ***Time-resolved SFX***

As mentioned before, we are in the new era of structural biology where new techniques are being developed to enable time-resolved studies in room-temperature conditions. In pump-probe experiments, crystals are activated with a trigger, e.g. a laser (the pump) which initiates a reaction inside the protein crystal. The state of the protein crystals is captured with an X-ray (the probe) after a specific time after laser pumping. There are other approaches to TR-studies, such as mix-and-inject serial crystallography (MISC) [81, 82]. MISC is suitable for e.g. studying enzymatic reactions by mixing protein crystals with a buffered substrate solution in a T-junction mixer, coupled to a GVDN. The MISC approach was recently used by Ishigami et al. [83], proposing the captured P<sub>R</sub>-intermediate structure of cytochrome *c* oxidase 8 seconds post-mixing. TR-experiments with MISC are limited by mixing- and diffusion rates and the demand for low-viscous mediums.

Pump-probe studies at synchrotrons have involved the Laue method, in which a polychromatic beam is shot at a stationary crystal, producing a Laue pattern with time resolutions up to picoseconds. The Laue method is not very practical due to radiation damage issues and the demand for large robust crystals [84]. In serial pump-probe crystallography experiments at XFELs, microcrystals are delivered in a jet by a GVDN- or LCP injector and a reaction initiated by a pump-laser as depicted in figure 9. At the pump stage, it is important that the laser triggers the protein population with high occupancy and without damaging the microcrystal. The laser spot size must be sufficiently big to cover the entire crystal for successful reaction triggering. The timing depends on the flow rate, the distance between the pump and probe and the timing jitter of the X-rays, which must be taken into account [85]. High repetition rate of the probe demands fast sample flow, which in turn put demands on a consistent, homogenous and reproducible sample jet. Fresh and uncompromised crystal sample must be delivered in time before the next XFEL-pulse, controlled by the sample flow rate. When consistent sample jetting is problematic, fixed-target-SFX is an alternative option.

Using a laser is a fast way of triggering reactions, and lasers at XFELs operate in the ns-fs regime. Pump-probe experiments are limited to proteins or ligands that are triggered by light [75, 86-88] or proteins that are modified by opto-genetics. Alternatively, the protein can be indirectly activated if caged- or photopharmacological compounds are soaked, co-crystallized or mixed with the crystals and released by laser irradiation [89].

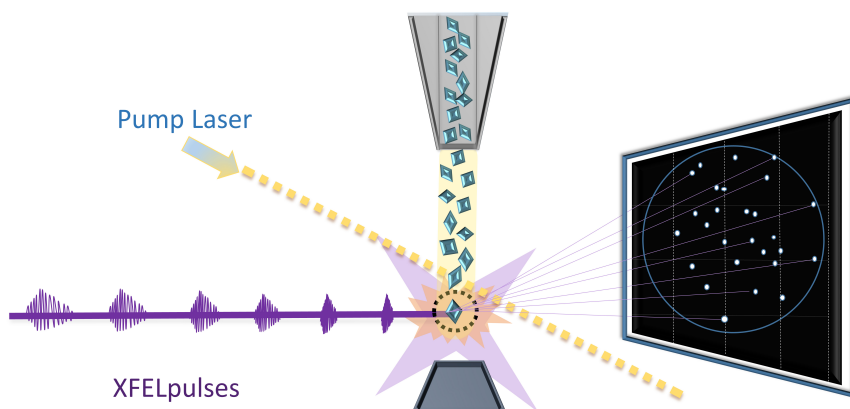


**Figure 9.** Basic view of the pump-probe set-up for serial femtosecond crystallography. The pump laser hits the crystal before the microcrystals reach the interaction point of the probe (XFEL-pulses). Diffraction images are collected by the detector (black pane) before the onset of radiation-damage induced destruction of the crystals.

## 5.5 Data processing with CrystFel and Structural Refinement

### *Differences between reflections from RX and SX*

In RX, data is collected by rotating the crystal while exposed to a monochromatic beam, giving a full set of reflections of the crystal (integration of the angle). In Laue crystallography, still images are collected from a stationary crystal which is exposed to a polychromatic beam (integration over the X-ray energy or wavelengths). Both RX- and the Laue methods provide full reflections, meaning that the full intensity of the diffraction spots are recorded [84].

Data collection strategy for serial crystallography differs from rotational crystallography. In SX, one still diffraction image is collected per crystal shot after exposure to a quasi-monochromatic beam, and the image contains almost only partial reflections of the crystal. In data processing aspects, these partial reflections do not cover enough of the crystal (the full angle for Bragg diffraction) to enable direct integration of the intensities to structure amplitudes. The solution to the partiality of SX is the collection of thousands of diffraction images that are integrated by the Monte-Carlo method, where the sum of all partial intensities is proportional to the square of the structure factor amplitude [90].

### ***Initial data processing at SACLA***

SX has the demand for systems that can sort out and integrate immense data quantities at fast rates and correctly deal with partial reflections and a quasi-monochromatic beam. This is why new software packages have been developed for handling of SFX-data. During a SFX experiment many thousands of crystals are shot at and even a larger number of images are collected; a frame is considered as a diffraction “hit” if there are  $\geq 15$ -20 peaks in it (this is an alterable software setting). Hit rates (number of diffraction patterns per recorded detector frames) can vary during an experiment due to physical conditions (clogging, beam flickering, weak crystals, sample inhomogeneity) but depend also on the software capacity of indexing multiple crystals per frame, yielding more efficient data collection than single-crystal snap shots [91]. Other parameters that are monitored on-line are the resolution and the number of peaks and saturated peaks. In processing the data collected at SACLA (paper I, III and IV), an adapted pipeline was used, divided into the *online* (real-time) and *offline* steps, followed by the *manual* steps for optimizing indexing parameters [92]. The pipeline include iterative spot finding, indexing and integration in order to reduce and refine the vast amount of data.

Online processing uses the program suite *Cheetah* [93] to monitor the hit rates, number of peaks, number of saturated peaks and resolution estimates in real-time. Subsequently, “offline” spot finding is performed by the *Cheetah Dispatcher* GUI. At this stage, hit images are converted into HDF5-files. The program suite CrystFEL [94] is incorporated in the *offline* pipeline. *Indexamajig* is part of the CrystFEL suite and repeats spot finding on the HDF5-files together with a detector geometry file. The geometry file provides information about physical data collection parameters such as dark current subtraction, masking pixels, detector saturation, gain adjustment, detector panels, photon energy, X-ray wavelength. Once hit images are found, they are autoindexed individually

(by invoking *DirAx* and/or *MOSFLM*). By viewing histograms of indexed images, one can find cell parameters for the majority of crystals. When indexing is successful, the images are integrated (spots are predicted) before a stream file is created of the results. The final information output of the offline steps are the unit cell parameters and knowing when the data has reached a sufficient number of indexable images (roughly  $\geq 10\,000$  images, but depending on the space group).

In the *manual steps* (that are not part of the pipeline), peak finding is executed again with *Indexamajig*. This time, refined parameters such as e.g. cell parameters, optimized detector metrology and beam center are given a priori to the program, which could potentially increase the indexing rate with 5-10% [92]. After indexing, a full reflection list is created with all the symmetry-related (equivalent) reflections merged together. Merging can be performed by the Monte Carlo method (*Process\_hkl*) where partialities are averaged and merged, or by scaling and post-refinement of all partialities (*Partiator*). After indexing, quality of the processed data is checked. *Completeness* and average signal strength  $I/\sigma(I)$  are calculated for the overall data and resolution shells by *check\_hkl*. Completeness is usually 100% in SFX experiments since the large number of reflections for one experiment cover all the possible unique reflections. *Compare\_hkl* takes two reflection lists and compare these to each other by  $R_{split}$  and Pearson's correlation coefficients  $CC_{1/2}$  and  $CC^*$ .  $CC_{1/2}$  is used for high resolution cutoff and predicts how precisely one half of the data set predicts the other by correlating the intensity values of the data sets (merged data) and should correlate with  $I/\sigma(I)$  [95]. [96]. After validating the data, the list of reflections are further processed by the *CCP4 software suite* [97]. By using *Truncate*, reflection intensities are converted to structure factor amplitudes, and transformed into electron density maps by obtaining the phases.

### ***Model building and refinement***

Model building and refinement is an iterative process, the goal being to build an accurate model into the electron density by adding residues and shaping the model so it fits the electron density, improving the phases of the model. Model building can be performed by the user in the GUI of *Coot* [98] (real-space refinement) while refinement by the program *Refmac5* is performed in reciprocal space [99]. *Refmac5* executes refinement of model parameters, such as [x y z] coordinates and temperature factors, but also under the control of different types of stereochemical restraints. After a refinement run in *Refmac5*, the job is evaluated by the R-factors (least square method)  $R_{work}$  and  $R_{Free}$  measuring

the error between experimentally observed and calculated structure factor amplitudes  $F_{\text{obs}}$  and  $F_{\text{calc}}$ . If the user did an accurate refinement job of the structure, meaning that the structure is correctly built into the electron density, the R-factors decrease consistently while the wrong model building increases the R-factors or increase the gap between  $R_{\text{work}}$  and  $R_{\text{Free}}$ . Electron density maps are calculated by combining the observed structure factor amplitudes by a Fourier series of  $|F_{\text{obs}}|$  together with the calculated phases from the  $\varphi_{\text{model}}$ .  $2F_{\text{obs}}-F_{\text{calc}}$  is usually calculated which is a combination of the direct map and difference map  $F_{\text{obs}}-F_{\text{calc}}$ , in which over- and under-modelled electron densities are coloured differently. The contour level decides how many details that are shown in the maps, but at the cost of noisiness.

### ***Difference electron density maps (time-resolved studies)***

In time-resolved experiments, difference electron density (DED) maps are calculated to track time-resolved conformational changes. As an example, a dark structure (pump-laser off) can first be refined into perfection before the structure factor amplitudes of the light state (pump laser on) are used to calculate the  $F_{\text{obs}}^{\text{light}} - F_{\text{obs}}^{\text{dark}}$  map. The observed structure factors from the dark data are subtracted from the light data, and the phases from the dark structure  $\varphi_{\text{dark}}$  are used for the DED maps, which is why a robust dark data set with accurate phases is of importance. Time-resolved structural changes are seen from the DED maps by detecting complementary negative and positive peaks.



### III. RESULTS AND DISCUSSION

## 6. Microcrystallization in LCP (paper I, II, III, IV)

The development of accurate tools and devices for handling the gel-like LCP matrix has made LCP more accessible to the world of protein crystallographers. When incorporating the LCP-method to the lab, lack of control was sensed in crystallization trials especially concerning microcrystallizations. Screening for novel microcrystallization conditions in a mosquito® crystallization robot [100, 101] using small volumes was a good start-off, but not suitable for big batch screening for LCP-microcrystals. Another tried method was to crystallize in Hamilton syringes, successfully used in previous studies of GPCRs [102, 103]. The syringe-based method gave us microcrystal hits (paper I) and opened up for the opportunity to collect data in a time slot of our collaborators beamtime (E. Nango and R. Tanaka). The urgency to obtain a sufficient sample volume forced us into trying something new, which was to crystallize in the wells of glass spot plates, facilitating crystallization in bigger batches. Luckily, the well-based procedure allowed for crystal growth at an early stage. Crystals prepared using both LCP microcrystallization approaches were used to collect the data for paper I.

### 6.1 Screening and producing microcrystals for SFX-experiments

The well-based method build on the same principles as described in [102] and [104]. The cubic phase is formed by mixing lipid+protein in 100- $\mu$ l Hamilton syringes, the ratios of lipid and protein being around 60:40 (when monoolein is used as lipid) to create a gel-like cubic phase which should be homogenous and transparent throughout the syringe [105]. A small string of created LCP (usually  $\sim$  5-7  $\mu$ l) is transferred to another Hamilton syringe that contains precipitant buffer with varying volumes (e.g. 10x the LCP-volume) [102, 106]. In studies of bacteriorhodopsin (bR), LCP-strings were dispensed into Eppendorf tubes instead of syringes, together with a thin metal wire facilitating crystal collection [75]. We encountered the need for a new type of microcrystallization method in order to produce the volumes needed for XFEL experiments, covered here.

**1. Monitoring the crystallization process:** The use of Hamilton glass syringes for microcrystallization trials in LCP were not convenient for monitoring of the crystallization progress using stereo microscopes, depicted in figure 10. When the LCP-string was positioned in an inconvenient place inside the syringe or out of plane, it was impossible to obtain a good focus of the crystal string. It was not possible to maintain a good focus at higher magnification to track the size, shape and quality of crystals. In order to properly characterize the crystals, the syringe had to be emptied from precipitant solution, adding a small volume of the LCP onto a microscope glass slide with a cover glass placed on top. This wasted the batch of produced microcrystals in that particular syringe if the crystals were not fully grown, limiting microcrystallizing of a protein for the first time or when having scarce amounts of protein. Another drawback was the time-consuming procedure of only being able to characterize  $\sim 5 \mu\text{l}$  of crystals at a time, meaning that the task had to be repeated for every syringe batch, consuming both time and crystal sample when squirting out some amount onto glass slides.

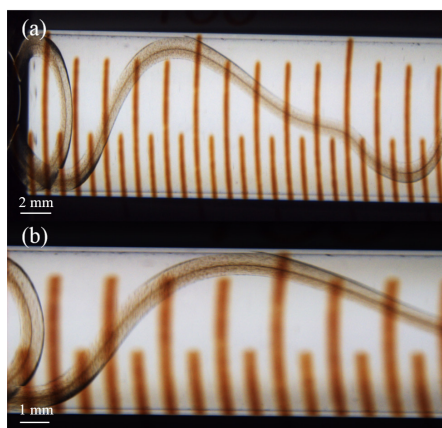


**Figure 10.** LCP crystallization in a 500- $\mu\text{l}$  Hamilton glass syringe visualized using a stereo microscope at (a) 7.5 magnification (b) 15 magnification (a). The shape, size and quality of the crystals are difficult to determine due to poor focus. *Figure from Acta Cryst. (2019). D75, 937-946*

**2. Batch-production of microcrystals:** The consumption of microcrystals in SFX-experiments are usually high, and the usage of GVDN-injectors demand much higher sample volumes than high-viscosity injectors, used

for e.g. LCP media. It may still be a laborious task to produce 1-3 milliliters of LCP-crystals if the aim of the experiment is to perform time-resolved studies in a pump-probe approach. Production of 3 ml microcrystals with  $\sim 5 \mu\text{l}$  LCP per syringe would mean 200-600 syringes must be set up to achieve desired sample volumes. An approach to increase the LCP-volume per syringe was injecting 5-15  $\mu\text{l}$  LCP (instead of 5  $\mu\text{l}$ ) into 500- $\mu\text{l}$  Hamilton syringes, filled with 300  $\mu\text{l}$  precipitation buffer (instead of  $<100 \mu\text{l}$ ) and by inserting multiple strings of LCP into a Hamilton syringe. This was a tricky scale-up and the success rate of incorporating multiple LCP-strings without plugging the syringe inlet was  $\sim 50\%$ .

### ***Procedure for well-based microcrystallization in LCP***

In order to circumvent the problems of visualizing microcrystals and the difficulty of producing large-batches in syringes, crystallization can conveniently be performed in the depressions of glass spot plates or even the wells of TPU-plastic plates. This is achieved by dispensing strings of LCP through a short needle to wells with precipitant solution as depicted in figure 11 and figure 12, and finishing by sealing with a plastic film (such as ClearVue plastic sheets, Molecular Dimensions). As seen in figure 11, crystals are easily visualized in the stereo microscope with high magnification, and crystal shapes and sizes are seen down to a few  $\mu\text{m}$  in size.

If crystallization conditions such as pH and salt-, protein- and precipitant concentrations are found, 2-dimensional screening with precipitant volumes vs. LCP-string volumes is valuable to find the conditions for optimal microcrystal size and density for individual proteins (see paper II for examples). Screening for precipitant volumes was done in 50-100  $\mu\text{l}$  steps and LCP-strings in 5- $\mu\text{l}$  steps. We found that protein- and precipitant concentrations had a greater impact on the crystal size and density than any other factor. In the case of *ba<sub>3</sub>*-type CcO, bigger crystals were obtained with increased protein concentration. Crystal size also increased with higher concentrations of precipitant (PEG 400), and concentrations  $>38\%$  transformed the LCP into a sponge-phase character [107] after a couple of days. We noticed a temperature-dependent crystal growth rate when monitoring the plates; crystals usually grew bigger and faster at temperatures  $> 20 \text{ }^\circ\text{C}$  (discovered after unintentional temperature rise in the lab environment); the phase was also less stable at these conditions. The monitoring and evaluation of crystal growth was non-laborious, time-efficient and convenient by the well-based LCP-microcrystallization method.

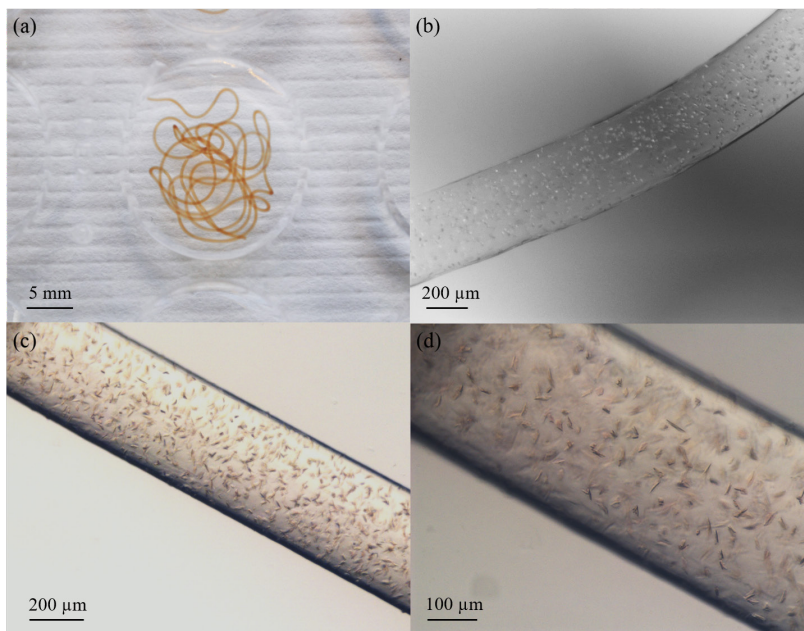


**Figure 11.** Well-based LCP microcrystallization. (a) A nine-well glass plate with an LCP string of 40  $\mu\text{l}$ . Microcrystals of *bas*-type cytochrome *c* oxidase (b) under polarized light at a magnification of 40 and at magnifications of (c) 50 and (d) 135. Crystal size, shape, quality and density can be clearly monitored over time. *Figure from Acta Cryst. (2019). D75, 937-946*

### ***Collecting microcrystals***

Microcrystal collection from wells was not a straightforward procedure at start. As for the results in paper I, microcrystals were collected by using a 1000- $\mu\text{l}$  pipette (Thermo Scientific™ Finnpipette) with a pipette tip. Crystals were sucked up together with a large excess of the mother liquor and dispensed into 500- $\mu\text{l}$  Hamilton syringes by the back of the syringe at the plunger position. This method was problematic since LCP adhered to the plastic of the pipette tips. Instead, it was tried to use the end tip of a plunger of a 100- $\mu\text{l}$  Hamilton syringe to collect LCP-strings with swirling movements that formed into a blob. The step-by-step procedure of collecting is depicted in figure 12. The blob was easily stuck to the end tip of the plunger, facilitating easy transfer of the LCP-blob into the back of a 500- $\mu\text{l}$  Hamilton syringe. A 500- $\mu\text{l}$  plunger was attached to the packed

500- $\mu$ l syringe and the LCP was pushed to the front end. In order to separate and remove residual precipitant solution, stacked LCP-blobs were pushed down with a 100- $\mu$ l plunger while the syringe was held vertically, (not shown in figure 12). Remaining precipitant solution could gently be removed by attaching a short needle to the packed syringe without collected LCP-crystals.

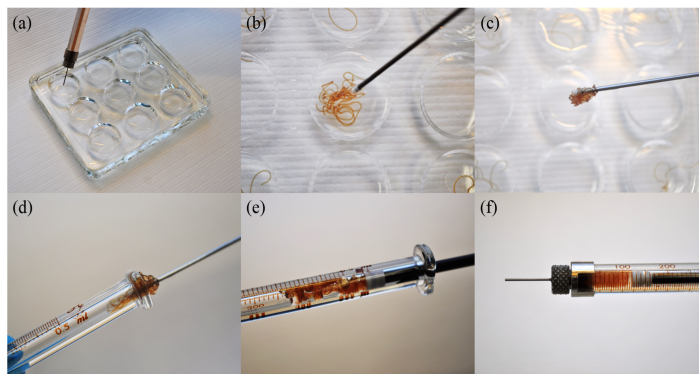


**Figure 12.** Well based crystallization and collection procedure. (a) A short needle connects to the LCP-syringe to dispense LCP-strings into the wells of a 9-well glass plate. (b) Microcrystals are collected with a plunger by swirling movements and different wells are pooled. (c) The LCP blob adheres to the plunger and (d) can be transferred to a 500 ml Hamilton syringe from the plunger positions. (e) A 500 ml plunger is inserted into the syringe (f) *ba*<sub>3</sub>-type cytochrome *c* oxidase crystals packed in a Hamilton syringe. *Figure from Acta Cryst. (2019). D75, 937-946*

### ***Screening for a non-toxic microcrystal condition in LCP***

The microcrystals of *ba*<sub>3</sub>-type CcO in paper I were yielded from a precipitant buffer containing sodium cacodylate at pH 5.3, which is an adapted microcrystallization condition from Tiefenbrunn et al. [108]. This arsenic-containing buffer is very toxic and created problems in crystallizations and data collection at SACLA. 2-(N-morpholino)-ethanesulfonic acid (MES) buffer is known to work as a good replacement for cacodylate (e.g. ICSG-plus™ HT-96 Eco Screen from Molecular dimensions). By well-based screening we confirmed that MES-buffer worked as a convenient alternative to cacodylate. The diffraction quality of the crystals were tested at SACLA, where collaborators E. Nango and R. Tanaka kindly spared us some of their beamtime to test the non-toxic

MES-condition. The microcrystals diffracted down to 2 Å and confirmed that the non-toxic condition could be used for future microcrystallization trials.

## **6.2 An enclosed system for CO-bound CcO in microcrystals**

In this work, we have developed a well-regulated system for producing and collecting data on microcrystals of reduced CO-bound *ba*<sub>3</sub>-type CcO to be used for SFX-experiments.

### ***Production of anaerobic and fully reduced microcrystals in LCP***

As for the native ligand O<sub>2</sub>, CO binds to a two-electron reduced catalytic site of CcO. The microcrystals of *ba*<sub>3</sub>-type CcO show an oxidized spectrum in the resting state (see paper I). Fully reduced crystals can be attained by adding artificial reductants such as sodium dithionite or ascorbate plus the mediator PMS and must be stored anaerobically to avoid oxygen turnover and oxidation. In order to keep anaerobic conditions, crystallization were mainly performed in an anaerobic glove box (AGB) (Coy Laboratory Product Inc). Two methods were tried out to obtain reduced microcrystals: either reduction of CcO prior to crystallization **(1)** or reduction of microcrystals after crystal formation **(2)**. All solutions including CcO, precipitation buffer, reductant etc. were purged with nitrogen before usage and entry into the AGB. Sodium dithionite was chosen as reductant since the crystals tolerated it well. In **(1)**, a well-based screen was performed which showed that the protein could be reduced with up to 20x[CcO] prior to crystallization without affecting microcrystal formation. Absorbance spectra of these crystals was measured by adding 2-3 µl of crystals to a CaF<sub>2</sub> glass cell that kept the crystals anaerobic. The spectrum of these crystals showed a mixture of oxidized and reduced states (a 414-nm oxidized peak was visible together with a broad heme *a*<sub>3</sub>-shoulder at 445 nm). Therefore, the crystals were further reduced by adding reductant to the mother liquor of the crystals with a final concentration of 1 mM, producing a fully reduced spectra of the CcO crystals. The reduced crystals were monitored over time and no shape-shift or anomaly was detected. In **(2)**, the anaerobically grown microcrystals were reduced by 1 mM sodium dithionite after crystal formation, which also produced a fully reduced spectrum of CcO. Method **(1)** was used throughout the crystallization process.

### ***CO-purging of reduced microcrystals***

CO-binding to fully reduced and anaerobic microcrystals of CcO can be achieved by purging with CO-gas. After crystallization and reduction by the well-based method, crystals were transferred together with the mother liquor into tubes or vials, sealable with septum. We used either chopped-off 15-ml plastic falcon tubes or 4-ml glass vials with septum. 1-2 ml of the mother liquor were transferred with 40-60  $\mu\text{l}$  of LCP-microcrystals to the tube and sealed with septum and parafilm, as depicted in figure 13. The air-tight samples were exited from the AGB and purged with CO-gas through the septum for 3-4 minutes (see figure 13). The microcrystals were not visibly damaged during the procedure. After CO-binding, the samples were entered to the AGB and incubated for 1 hour. The crystals were then collected from the tubes by the same procedure as described for the well-based method. Speed was of the essence in collecting the microcrystals in order to avoid CO-diffusion out from the microcrystals. Time-tests indicated that CO-bound crystals could be exposed to the AGB-atmosphere for 60-90 seconds without losing CO by diffusion. As seen in the spectra of figure 14, the time slot seemed safe for collecting crystals from the CO-purged tubes and transferring them to gas tight Hamilton syringes. The syringes were sealed with ferrules, plugs of parafilm and metal caps. The absorbance spectra was recorded to ensure that the packed crystals remained CO-bound (figure 14), and unbroken syringes stayed CO-bound for at least 5 days.



**Figure 13.** *Left:* A chopped-off falcon tube with a fitted septum that is penetrated by an inlet- and outlet needle. *Right:* An airtight cell of CaF<sub>2</sub>-glass which can be used to collect UV-Vis absorption spectra of microcrystals. The grey arrow indicates the cavity where the sample is positioned.

### ***Sample homogenization, topping up with CO, and injector loading***

Data of CO-bound crystals were collected at SACLA, and the facility kindly provided for an AGB where sample preparation and injector loading were handled. The crystal samples were homogenized with monoolein before loaded into the injector. Monoolein was melted at 40 °C, aliquoted into vials having septa and purged with CO-gas for 3 minutes before mixing with the LCP-crystals. CO-bubbled monoolein was added in 3- $\mu$ l aliquots to the crystals by union couplers and 100- $\mu$ l Hamilton syringes. When the LCP had a smooth and homogenous consistency mixing was sufficient. The crystal-containing syringe was mounted to an adapter, containing the sample cartridge where up to 60  $\mu$ l of CO-crystals were applied. To avoid air bubbles, the crystals were spun down for ~ 10 seconds in a micro-centrifuge before the sample cartridge was attached to the injector. A fully assembled injector had one opening at the extrusion end of the nozzle, allowing CO to diffuse out from the microcrystals. In order to avoid CO-diffusion, the sample-facing side of the nozzle was covered with vacuum grease, which could be extruded when initiating data collection. An oxygen test for the grease-sealed injectors showed that no oxygen leaked into the sample environment of the cartridge, depicted in figure 14. The assembled high-viscosity injector and an oxygen indicator tablet were placed in a gas-tight plastic bag and heat-sealed before exited from the AGB. The oxygen indicators showed that the interior of the plastic bag was kept oxygen free for several hours.

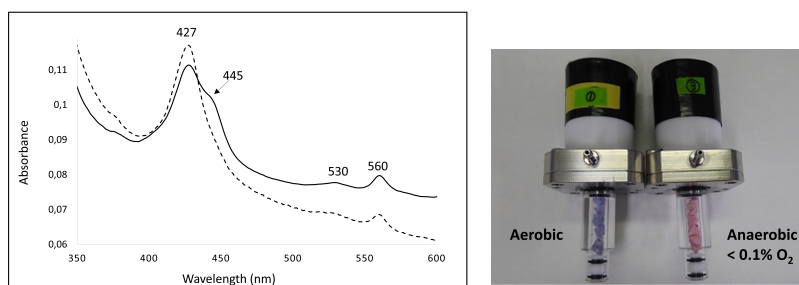


**Figure 14.** *Left figure:* Optical absorbance spectra of collected *bas3*-type CcO microcrystals in Hamilton syringes. The spectra for 1 mM dithionite-reduced microcrystals (solid line) and reduced CO-bound microcrystals (dashed line).

*Right figure:* Sample cartridges containing oxygen indicators, mounted to nozzles for high-viscosity injectors at SACLA. The left injector is not sealed with vacuum grease having an aerobic environment, as detected by the blue color of the oxygen indicator. The right injector is sealed with vacuum grease and has less than 0.1 % oxygen in the sample environment as seen by the pink color of the indicator.

### **6.3 Summary**

The well-based method for producing microcrystals in lipidic cubic phase enables convenient monitoring of the crystallization process and large-batch production of microcrystals in LCP. The well-based method was used to find a non-toxic microcrystallization condition for *ba*<sub>3</sub>-type CcO and novel microcrystallization conditions for sensory rhodopsin II and bacterial reaction center (papers II-III) in LCP. The need for efficient microcrystallization strategies in LCP will grow with the accessibility of SX-beamtimes at XFELs and 4:th generation synchrotrons. The presented method provide for convenient handling of microcrystals and allow alterations of the microcrystal environment with real-time monitoring. The handiness of adding chemical compounds and purging microcrystals is elaborated here, focusing on producing reduced CO-bound microcrystals of *ba*<sub>3</sub>-type CcO.

## 7. Room-temperature SFX-structure of $ba_3$ CcO in the resting state (paper I)

In paper I, we present the first room-temperature SFX structure of CcO, free from radiation damage. A structural analysis is presented of the active site ligand, in which we propose a single-oxygen species is bound. The overall structure and the functional domains of CcO are compared to previous cryogenic structures that were determined at cryogenic temperatures.

### 7.1 Room temperature data collection of $ba_3$ -type CcO in the resting state

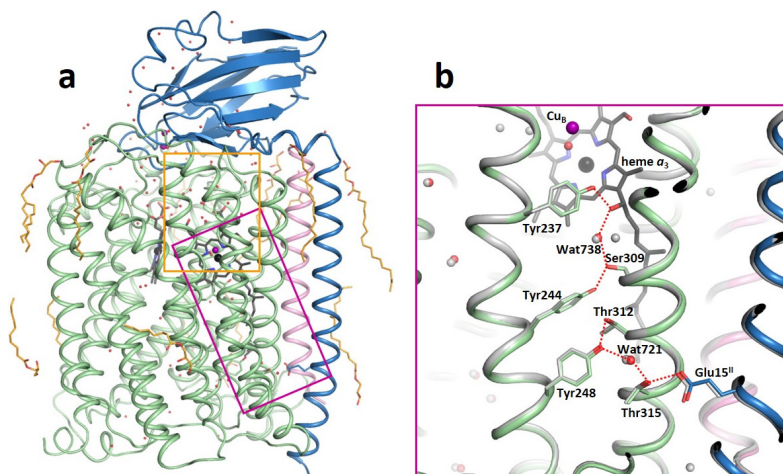
Data on microcrystals of  $ba_3$ -type CcO in LCP were collected at SACLA by usage of the high viscosity injector described in [75] at a flow-rate of 0.48  $\mu\text{l}/\text{min}$ , and 25  $\mu\text{l}$  of microcrystal sample yielded a complete diffraction data set in 50 minutes. The XFEL photon energy was at 7.6 keV and the pulses were  $\sim 10$  fs in duration. 87,057 frames were collected in total, of which 13% were considered as hits by Cheetah [93] and 8,211 being indexed and merged by CrystFEL [94]. The phases were calculated by Phaser [109] and the cryogenic LCP-structure of Tiefennbrunn et al. [108] (PDB ID 3S8F) was used as model. The presented structure was refined to a resolution of 2.3  $\text{\AA}$ .

### 7.2 SFX structure of $ba_3$ -type CcO free from radiation damage: comparison to a cryogenic LCP structure

The microcrystallization conditions of our SFX structure were derived from the published cryo-LCP-structure from Tiefennbrunn et al. [108] that diffracted to 1.8  $\text{\AA}$ , and their model was as also used to calculate the phases of our model. The two structures show good agreement between each other regarding unit cell parameters, space group (C2) and the  $C_\alpha$  root mean-square deviation (0.32  $\text{\AA}$  in comparison). Due to lower resolution of the data and higher entropy at room-temperature, we detect less water molecules and lipid tails. The overall structure is showed in figure 15. 92 water molecules and thirteen lipids molecules were modelled in the room-temperature structure compared to 225 waters and twenty lipids identified in the cryo-LCP structure. Two newly found lipid tails associated to subunit I were localized in our SFX structure.

Proton transfer is one of the fundamental functions of CcO, and in  $ba_3$ -type CcO there is only one path leading protons from the N-side to the active site for water formation or leading protons to be pumped across the

membrane. The proton path comprising of polar amino acids and waters, is identical in our SFX structure compared to the cryo-LCP structure as shown in figure 15. A cavity in the proton pathway is present in our SFX structure as well as in the cryo-LCP structure and previously published structures of *ba*<sub>3</sub>-type CcO [110]. The gap is 4.45 Å, located between Threonine-312 and Tyrosine-244. This cavity makes the proton pathway non-functional, and a dynamic element ought to exist which transiently makes proton translocation possible. This functional component can e.g. be a mobile water molecule, temporary creating the necessary linkage between the two polar amino acids upon proton uptake from the N-side. The K-path analogue starts at glutamate-15 in subunit II, and further via threonine-315, a water molecule numbered wat-721, tyrosine-248, threonine-312, tyrosine-244, serine-309, wat-738, heme *a*<sub>3</sub>'s secondary alcohol and finally to tyrosine-237 which is located close to the active site [111].



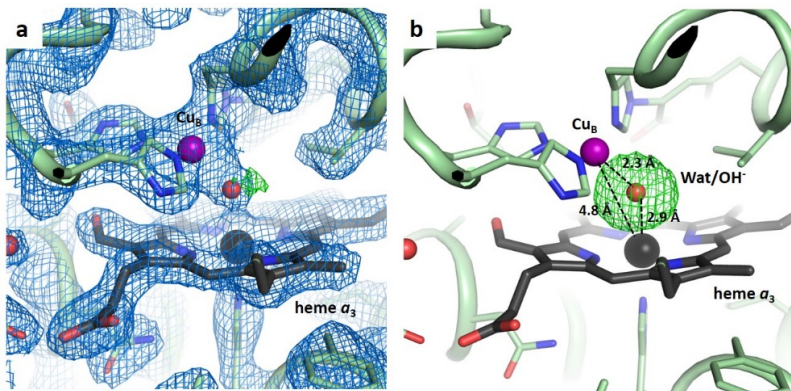
**Figure 15.** Serial femtosecond structure of *ba*<sub>3</sub>-type CcO at room-temperature. The amino acid numbering refers to *ba*<sub>3</sub>-type CcO (a) Overall structure with subunit I in green, subunit II in blue and subunit IIIa in pink . The pink square represents the proton path and yellow the proposed proton loading site (b) The K-path analog for protons in *ba*<sub>3</sub>-type CcO. The SFX structure is shown in green/blue/pink and the cryo-LCP structure (PDB code 3S8G) is shown in grey. Water molecules are shown in red (SFX) and grey (cryo-LCP).

Figure from *Scientific Reports* 7, 4518 (2017)..

### 7.3 Structural differences at the active site and the proton loading site

The redox state of the microcrystals of  $ba_3$ -type CcO were investigated by absorbance spectroscopy (procedure described in previous chapter), confirming the crystals were in the fully oxidized state. In paper I, we list all the deposited structures of  $ba_3$ -type CcO and their active-site ligands, of which only three (1EHK[13], 1XME[112] and 3EH4[113]) deposit a water-ligated state. The majority have either no ligand [113-115] or a peroxide modeled in the active site ([108],[116] and 12 unpublished structures by Li, Y., Chen, Y., Stout, C.D. A peroxide ion  $O_2^{2-}$  was built into the active site, owing to the elongated shape of the unbiased difference density. As seen in figure 16, a round-shaped  $F_o-F_c$  difference density is evident in our presented SFX structure, which reveals that a single oxygen species such as  $H_2O$  or  $OH^-$  is likely ligated there. When modelling a water molecule to the active, very little residual difference density is unaccounted for. We compare the residual density to the  $F_o-F_c$  densities in a cryogenic-LCP structure of  $ba_3$ -type CcO [108] and a bovine  $aa_3$ -type CcO from an XFEL-cryogenic model [117] after exchanging their peroxide ligands into a water molecule, depicted in figure 17. As illustrated, much larger residual  $F_o-F_c$  densities remain in the cryogenic structure of CcO comparing to the SFX-structure presented in this work. These findings indicate that a modelled water or hydroxide is a good fit for our presented SFX-structure but not well-suited in the cryogenic structures of CcO. Our statement is further supported by a comparable peak-height between the modeled water in the BNC ( $0.99 e^-/\text{\AA}^3$ ) and a tightly bound water molecule located between the secondary alcohol of heme  $a_3$  and serine-309 ( $0.86 e^-/\text{\AA}^3$ ). The peak heights are compared from the same electron density and therefore no consideration of different background contributions from solvent is needed.

Further, it has been argued against a modeled peroxide ion ( $O_2^{2-}$ ) in the oxidized active site of CcO by Kaila et al. [118] using DFT calculations, spectroscopy and re-refinement of crystallographic data. Kaila et al. solely investigated the  $aa_3$ -type CcOs, and argue that it is likely that the elongated electron density is attributed to a molecular superoxide ion  $\bullet O_2^-$  (supported by the DFT calculations) or an X-ray reduced  $O_2$  molecule that is converted to a superoxide ion,  $\bullet O_2^-$ . A bound peroxide to the BNC would not be stable since it generates the short-lived  $P_M$  reaction intermediate, while a bound superoxide would be more stable, shown by their calculations.



**Figure 16.** Active site structure of the  $ba_3$ -type CcO from SFX data modelled with a water molecule or a hydroxide ion bound. (a) The  $2F_o-F_c$  density (blue) is contoured at  $1.5 \sigma$  and the  $F_o-F_c$  difference density (green) at  $4.0 \sigma$ . (b) The unbiased  $F_o-F_c$  omit map density is contoured at  $4.5 \sigma$ . *Figure from Scientific Reports 7, 4518 (2017).*

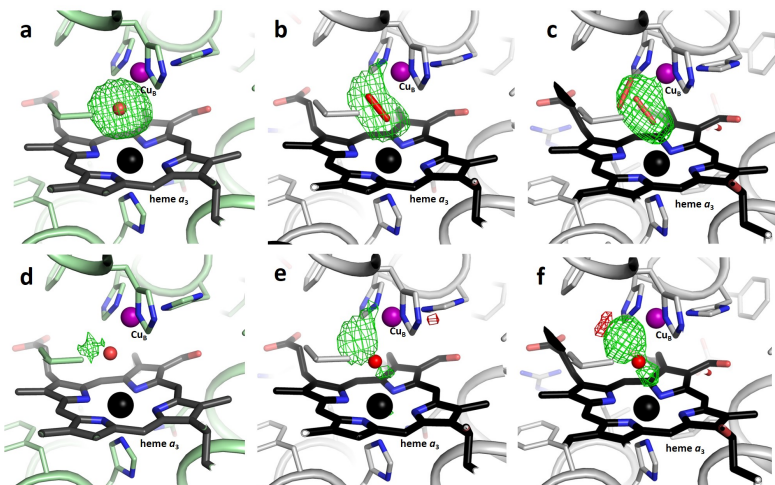


**Figure 17.** Active site electron densities, with bound oxygen species shown in red. (a–c) Unbiased  $F_o-F_c$  omit map densities (green) contoured at  $4.5 \sigma$ , calculated without ligands for (a)  $ba_3$ -type CcO from SFX data (b)  $ba_3$ -type CcO from cryo-LCP data (PDB code 3S8G). (c) bovine heart  $aa_3$ -type CcO from XFEL data of large crystals at cryo temperature (PDB code 3WG7), two bound peroxide molecules with partial occupancies are shown in red. (d–f)  $F_o-F_c$  difference densities calculated with a water molecule bound shown in green (positive) and red (negative) contoured at  $+4.0/-4.0 \sigma$ . (d)  $ba_3$ -type CcO from SFX data. (e)  $ba_3$ -type CcO from cryo-LCP data (PDB code 3S8G). (f) bovine heart  $aa_3$ -type CcO from XFEL data of large crystals at cryo temperature (PDB code 3WG7). *Figure from Scientific Reports 7, 4518 (2017).*

### ***Structural differences around the proton-loading site***

Since proton pumping is coupled to redox-chemistry at the active site, it is reasonable to believe a structural motif (in proximity) is responsible for proton pumping. It has been proposed that the heme  $a_3$  propionates [111], surrounding water clusters around the propionates or an aspartate (asp-372 in  $ba_3$ -type CcO) are involved [119] in proton pumping. With certainty, proton pumping is more efficient in the  $aa_3$ -type CcOs. A structural motif, missing in the  $ba_3$ -type CcO, is a magnesium ion affecting proton affinity around the water constellations, seen in figure 18. In  $ba_3$ -type CcO, the magnesium ion is exchanged for a carboxyl group of glutamic acid-126 in subunit II. Another difference, presumably coupled to diminished proton pumping in  $ba_3$ -type CcO, is the lack of a tryptophan radical formed in  $aa_3$ -type CcO, shown to be important for proton pumping in  $aa_3$ -type CcOs [120].

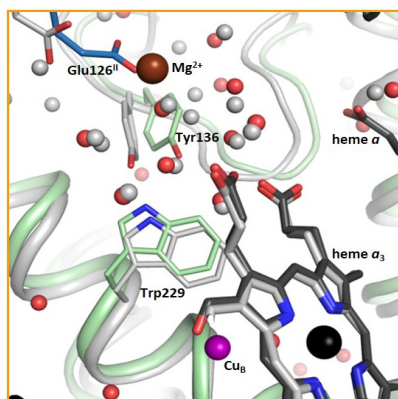


**Figure 18.** The alleged proton-loading site in  $ba_3$ -type CcO and bovine heart  $aa_3$ -type CcO. The SFX structure is shown in green/blue and the bovine structure (PDB code 3WG7) in grey. The magnesium ion is shown in brown which belongs to the bovine structure. Water molecules are shown in red (SFX) and grey (bovine heart). Heme  $a_3$  is shown in black (SFX) and grey (bovine heart). *Figure from Scientific Reports 7, 4518 (2017).*

## **7.4 Summary**

We propose the ligand of  $ba_3$ -type CcO in the oxidized resting state to be different from previously published structures. The room-temperature SFX structure of CcO is presented here, free from radiation damage, since the average X-ray dose of 13 MGy per microcrystal is considered as

insignificant to produce local or global X-ray induced damage in the femtosecond time range [121, 122].

Our structure clearly show a spherical positive peak in the  $F_o-F_c$  electron density. The unbiased difference density indicate a bound water or hydroxide ion ( $\text{OH}^-$ ) ligated to the *heme a<sub>3</sub>*- $\text{Cu}_B$  site in the oxidized resting state. Due to the overall positive charge of BNC at this state ( $\text{Cu}^{2+}$  and  $\text{Fe}^{3+}$ ), hydronium ions ( $\text{H}_3\text{O}^+$ ) are not likely to bind despite the low pH of used crystallization conditions (pH 5.3), and more likely a hydroxide ion binds. Comparisons were also made of the unbiased  $F_o-F_c$  maps in the active site of our SFX-structure and previous oxidized CcO-structures, where active site ligands were exchanged for a water molecule and residual densities compared. The results in paper I give further tools and provide the foundation to study the reaction cycle of CcO by time resolved SFX, contributing to elucidate proton pumping in all cytochrome *c* oxidases.

## 8. CO-complexed *ba*<sub>3</sub>-type CcO deduced by serial femtosecond crystallography (paper IV)

The application of XFELs in structural biology have set the ground for the first structures of CcO which are free from radiation damage. With these advancements, more details are being revealed about the structural motifs that are involved in coupling the electron transfer reactions to proton pumping in CcO. Structures of bovine *aa*<sub>3</sub>-type CcO have been deposited with carbon monoxide (CO) bound and dissociated from the active site [123, 124], along with a time-resolved reaction intermediate of CcO [83]. CO binds to the reduced binuclear site of CcO similarly to its native ligand O<sub>2</sub>, and it is assumed that CO initiates the same conformational changes upon binding as O<sub>2</sub> does. CO is however not an electron and proton acceptor and does not initiate proton pumping upon binding to CcO. Recent studies of bovine CcO have revealed that CO-binding to the reduced active site triggers major changes in the side chains of an helix fragment (helix X) which is located between heme *a*<sub>3</sub> and heme *a*. Here, the first CO-bound structure of *ba*<sub>3</sub>-type CcO at room-temperature is presented, which is free from radiation damage. We suggest that a structural transition in helix X does not occur upon CO-binding in *ba*<sub>3</sub>-type CcO as opposed to bovine CcO, indicating that *ba*<sub>3</sub>-type CcO differs from *aa*<sub>3</sub>-type CcO in the structural transitions associated with ligand binding to the active site and possibly also to proton pumping.

### 8.1 SFX-data collection, processing and structural refinement

The procedures of producing, collecting and injecting CO-bound microcrystals of *ba*<sub>3</sub>-type CcO at anaerobic conditions are elaborated in previous sections (chapters 3 and 5).

SFX diffraction data of CO-bound CcO were collected at the BL3 beamline of SACLA. Microcrystals in LCP were added to a high-viscosity injector as described in section 5.2 and mounted to the DAPHNIS platform [77] consisting of a sample chamber with helium gas environment and a MPCCD detector [80] where the sample-to-detector distance was 50 mm. The microcrystals in LCP were jetted at a flow rate of 0.5-1.5  $\mu$ l/min into the XFEL-beam. The crystals were probed with X-ray pulses of 7.5 keV in photon energy, having a repetition rate of 30 Hz and a pulse duration below 10 fs. Diffraction images were processed according to the established pipeline at SACLA using Cheetah and CrystFEL as described in previous sections. A number of 201,274 images were collected which contained 41,059 diffraction hits, of which 60.4% were successfully

indexed (see table 1 in paper IV). Molecular replacement with Phaser [109] was used to solve the phases with our oxidized structure (PDB ID 5NDC) as search model, and refinement was performed by Refmac5 with an upper resolution limit at 2.0 Å [99].

## 8.2 SFX structure of reduced CO-bound *ba*<sub>3</sub>-type CcO at room temperature

The electron density in the unbiased  $F_o-F_c$  omit maps of our presented CO-bound SFX structure shows a large elongated shape in the active site of CcO, depicted in figure 19 a. Consistently, our previous SFX-structure of oxidized CcO showed a spherical shape of the unbiased  $F_o-F_c$  omit maps (PDB ID 5NDC), from which we concluded that a single-oxygen species such as a hydroxide ion or a water was bound (figure 19b). The peak height of the elongated density in the active site which attributed to a bound CO, is much higher than the electron density feature of a conserved water molecule, supporting the conclusion that a hydroxide or water is not a probable ligand in the presented structure here. Also, after modelling a water into the positive peak of the active site (figure 19 c) a large elongated residual density remains at a contour level of  $\sigma=4.5$ , which also contradicts a bound single-oxygen species in the structure presented here. After modelling a CO-molecule in the active site, small residual density remains at a sigma level of 3.5 after refinement and no residual density remains at a sigma level of 4.5. The maps show an accurate fit of a carbon monoxide molecule ligated to the Fe in the binuclear heme  $a_3$ -Cu<sub>B</sub> site with binding distances of 1.96 Å and 2.26 Å for Fe-C<sup>CO</sup> and Cu<sub>B</sub>-O<sup>CO</sup> respectively and a Fe<sub>a3</sub>-C<sup>CO</sup>-O<sup>CO</sup> angle of 139°. Further, we know from UV-Vis absorbance spectroscopy that the microcrystals were fully reduced and CO-bound prior to injector loading also confirming a CO-ligated state of CcO.

Our SFX structure of CcO-CO show rather similar binding geometry to a previous (and solely deposited) cryogenic synchrotron structure of *ba*<sub>3</sub>-type CcO-CO at 2.9 Å resolution (PDB ID 3QJQ), seen in figure 20 a. The unbiased  $F_o-F_c$  omit map of the cryogenic structure does not show a distinct shape in the positive peak at the active site, but looks rather smeared between the Fe- and Cu<sub>B</sub>. The model of the cryogenic CcO-CO structure shows ligation of CO to both heme  $a_3$  and Cu<sub>B</sub>.

The binding geometry of CO and the unbiased  $F_o-F_o$  omit electron densities were also analyzed for two different structures of CO-bound bovine CcOs, both presumably being free from radiation damage, depicted in figure 20 (PDB IDs 5W97 and 5X1F). One of the CO-bound structures was deduced by SFX (5W97) and displays binding distances of 1.89 and 2.74 Å for Fe-C<sup>CO</sup> and Cu<sub>B</sub>-O<sup>CO</sup> respectively and a Fe<sub>a3</sub>-C<sup>CO</sup>-O<sup>CO</sup> angle of

141° [123]. Corresponding values for an XFEL-structure of CcO-CO collected at 5°C using a number of larger crystals that were translated every few images (5X1F) were 2.14 Å, 2.38 Å and 135° [87]. The redox-state of 5X1F was monitored by absorption spectroscopy, which showed a CO-bound state of CcO before and after data collection. The two bovine CcO-CO structures however show different shapes of the unbiased omit electron densities and different positions of CO in the active sites, as depicted in figure 20. It is unclear why the conformation of CO differ in the two bovine structures, considering equivalent heme  $a_3$ -Cu<sub>B</sub> configurations, absence of radiation damage and identical space groups of the two bovine structures. Muramoto et al. deposited CO-bound synchrotron structures of bovine CcO collected at 100 K and 280 K (-173 °C and 7°C) where they demonstrate a clear difference in the CO-binding configuration between the structures [125]. In the structure collected at 280 K, carbon monoxide display a bent configuration (PDB ID 3AG1) which is similar to the CO-configuration in the SFX structure mentioned previously. This could be due to partial dissociation of CO at room temperature. In the structure collected at 100 K (3AG2), CO adopts a flat configuration.

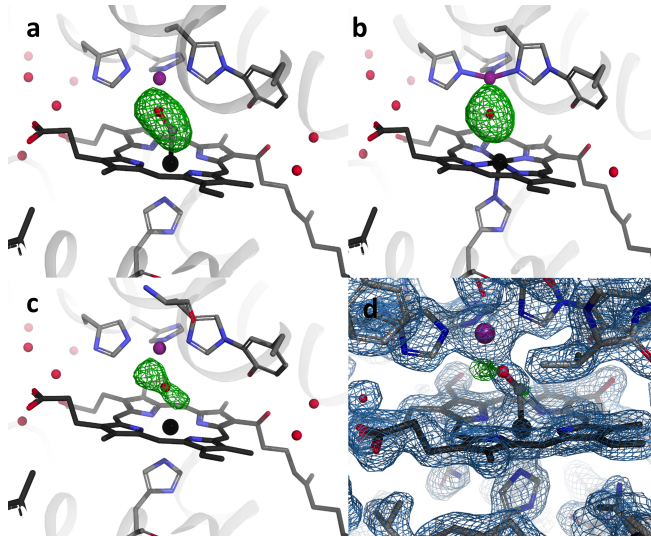


**Figure 19.** Active site structure of *ba*<sub>3</sub> CcO with the F<sub>o</sub>-F<sub>c</sub> omit density in green calculated without the active site ligand, contoured at 4.5  $\sigma$  in (a-b). (a) Reduced CO-bound state from SFX data. (b) The oxidized structure (PDB ID 5NDC). (c) F<sub>o</sub>-F<sub>c</sub> difference density calculated with a water bound in the reduced CO-bound state from SFX data. (d) The reduced CO-bound structure with a CO molecule bound in the active site. The 2F<sub>o</sub>-F<sub>c</sub> density (blue) is contoured at 2  $\sigma$  and the F<sub>o</sub>-F<sub>c</sub> density (green) is contoured at 3.5  $\sigma$ .

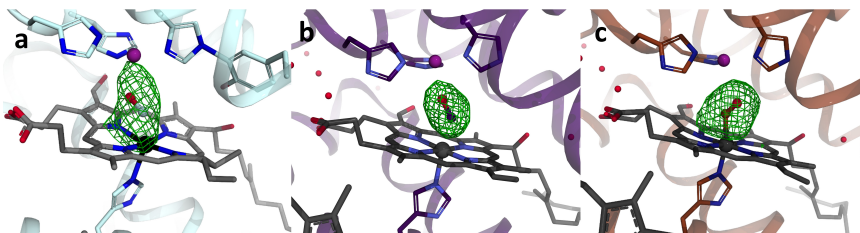


**Figure 20.** Structures of CcO in the reduced CO-bound state with F<sub>o</sub>-F<sub>c</sub> omit map densities at the active site calculated without CO are displayed at 4.0  $\sigma$ . (a) *Ba*<sub>3</sub>-type CcO structure solved from synchrotron data collected at cryogenic temperature (PDB ID 3QJQ). (b) Bovine CcO structure solved using XFEL data from larger crystals that were translated every few images collected at 5 °C (PDB ID 5X1F). (c) Bovine SFX-structure of CcO collected at room temperature (PDB ID 5W97).

### 8.3 Structural comparison of the CO-bound, oxidized and reduced states of $ba_3$ -type CcO

The CO-bound SFX structure of  $ba_3$ -type CcO presented here demonstrates very little structural variations compared to the oxidized SFX structure of  $ba_3$ -type CcO presented in paper I. Our CcO-CO structure displays 156 water molecules and 12 lipids compared to 58 waters and 22 lipids in the oxidized SFX structure. Localized differences can though be seen between the presented structure of CcO-CO and a reduced structure of  $ba_3$ -type CcO (CcO-red), referring to a cryogenic synchrotron structure (PDB ID 3EH5, 2.8 Å) [44]. These differences are displayed around the K-path analogue (threonine-315 and glutamate-15II), the BNC ligating histidine residues and the proposed proton loading site located around the propionate chains of heme  $a_3$ , asparagine-366, aspartate-372, glutamate-126, arginine-225 and arginine-449 ( $ba_3$ -type CcO numbering). However, we cannot rule out that the structural differences between CcO-CO and CcO-red are a result of the differences in experimental conditions. The fact that no actual differences are seen between the room-temperature SFX structures of oxidized CcO and CcO-CO also motivates to compare the CcO-CO structure with a room-temperature SFX structure of reduced  $ba_3$ -type CcO currently absent in the PDB.

### 8.4 Structural alterations of helix X in $aa_3$ -type CcO are absent in $ba_3$ -type CcO

In paper IV, we discuss deposited structures of bovine CcO which are CO-bound and also have CO dislodged from the active site. One of these studies compare a structure of CcO-CO (determined by SFX) to a cryogenic synchrotron structure showing X-ray induced CO-movement (5WAU). Another study compares an XFEL structure of CO-bound CcO with two flash-photolysed structures collected 20 ns and 100  $\mu$ s after pump-laser initiation (5X1B and 5X19 respectively). Both studies show the presence of a structural transition, occurring when CO binds to the reduced state of CcO [125, 126]. Some of these findings are also in line with structural redox-transitions seen in  $aa_3$ -type CcO in *R. Sphaeroides* [127]. The structural movements in  $aa_3$ -type CcOs are a shift of heme  $a_3$  upon ligand binding or a redox-state conversion, which is accompanied by a shift in a stretch of residues in helix X. Helix X is a highly flexible region located between heme  $a$  and heme  $a_3$  in  $aa_3$ -type CcO. Distinct transitions occur especially for a serine residue (Ser382 in bovine and Ser425 in *R. sphaeroides*) and a valine in bovine CcO (Val380) as depicted in figure 21. In paper IV, we compare helix X of CO-bound and reduced  $ba_3$ -type

CcO in the light of the changes that occur in bovine CcO. *Ba*<sub>3</sub>-type CcO does not contain the highly flexible valine and serine residues; these are exchanged for glutamine and alanine respectively and do not undergo structural transition. There are no structural transitions observed within the helix X region when comparing CcO-CO and CcO-red in *ba*<sub>3</sub>-type CcO as displayed for *aa*<sub>3</sub>-type CcO. Therefore we suggest the *ba*<sub>3</sub>-type differ from *aa*<sub>3</sub>-type CcO in the structural transitions occurring upon ligand binding, which in extension indicate possible differences in proton pumping mechanisms between the two classes. This assumption is not unlikely, considering the different proton pumping stoichiometry of *aa*<sub>3</sub>- and *ba*<sub>3</sub>-type CcOs.

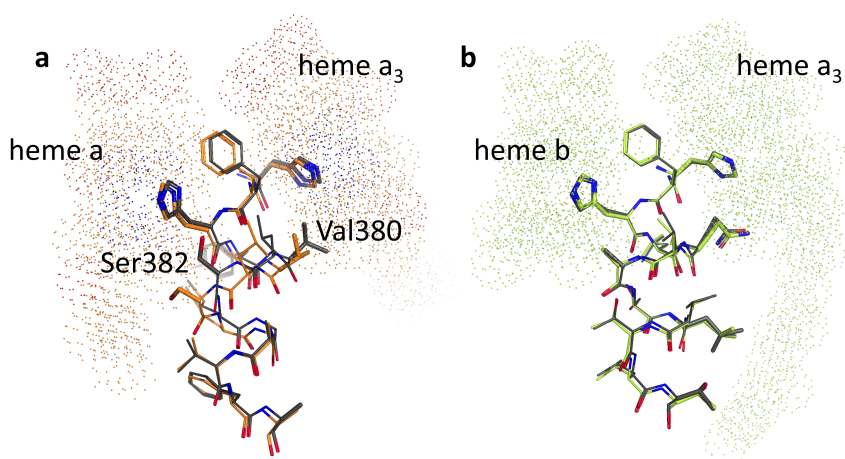


**Figure 21.** Overlaid structures of the reduced and CO-bound states zoomed in on the helix X segment of (a) bovine *aa*<sub>3</sub>-type CcO and (b) *ba*<sub>3</sub>-type CcO. Heme *a*, heme *b* and heme *a*<sub>3</sub> are located in the dotted regions. (a) The reduced bovine CcO structure from synchrotron data at cryo temperature (PDB ID 5XDX, grey) overlaid on the reduced CO-bound bovine CcO structure from XFEL data collected at 5 °C (PDB ID 5X1F, orange). (b) The reduced *ba*<sub>3</sub>-type CcO structure from synchrotron data at cryogenic temperature (PDB ID 3EH5, grey) overlaid on the reduced CO-bound *ba*<sub>3</sub>-type CcO structure from room-temperature SFX data collection presented here (green).

## 8.5 Summary

We present the first room-temperature SFX-structure of *ba*<sub>3</sub>-type CcO in complex with carbon monoxide, free from radiation damage (paper IV).

The CO-binding geometry of the presented structure is compared to bovine CcO in CO-complex, for which data were collected under different conditions and by different methods. It appears the CO-configuration is sensitive to different data collection conditions used.

A flexible structural motif denoted helix X, was previously identified in *aa*<sub>3</sub>-type CcO (bovine and *R. sphaeroides*) undergoing a structural transition from the reduced- to the CO-bound state. This transition is however not seen for *ba*<sub>3</sub>-type CcO in the corresponding region when comparing the presented CO-bound SFX-structure to a reduced structure (PDB ID 3EH5) collected by synchrotron radiation at cryogenic conditions. Our observations could be strengthened by comparing the presented CO-bound SFX-structure to a reduced structure of *ba*<sub>3</sub>-type CcO determined by SFX. The addition of on-line absorbance measurements during data collection would further support the CO-bound state of the X-ray exposed microcrystals in paper IV. This work revises the differences between *ba*<sub>3</sub>- and *aa*<sub>3</sub>-classes of CcO regarding the structural events that occur upon CO-binding, which could possibly explain the different proton pumping characteristics among classes CcO.

## 9. Initial results from pump-probe SFX with dissociation of CO from the active site of $ba_3$ -type CcO

We aimed to study CO-dissociation from the active site of CcO by pump-probe SFX experiments, possible due to the fact that carbon monoxide can be photo-dissociated from the active site using a short 532 nm laser pulse. Structural changes followed by pump laser irradiation could reveal the reversed structural transitions occurring when O<sub>2</sub>-binds to the active site of CcO. Two pump-probe structures of CO dissociation from CcO were previously deposited, collected at 20 ns and 100  $\mu$ s after laser pumping [124]. Moreover, structures of CcO were deposited where CO was dislodged from the active site as a consequence to irradiation by X-rays or surrounding light sources [44, 128]. However, the majority of pump-probe studies of CcO complexed to CO have been solution-based, see [129-132] for a small selection of spectroscopic studies.

### 9.1 Pump-probe data collection, processing and generation of initial difference electron density maps

Diffraction data of  $ba_3$ -type CcO-CO in LCP were collected at 500  $\mu$ s ( $\Delta t_{\text{light}} = 500 \mu\text{s}$ ) and 2 ms ( $\Delta t_{\text{light}} = 2 \text{ ms}$ ) after pump laser irradiation and at two different laser powers, 100  $\mu$ J and 200  $\mu$ J. The required laser power was estimated by comparing with time-resolved pump-probe experiments of bR in LCP [75, 133]. Data were collected in an interleaved 1:2 fashion for all time points: light (laser on), dark1 (laser off) and dark2 (laser off). This data collection strategy is particularly good in order to avoid light contamination in the dark images. The images were classified as dark or light with Cheetah, and a large dark data set was collected to obtain accurate phases for the difference electron density (DED) map calculations (see table 1 in paper IV for the dark data statistics). The images were indexed and merged by CrystFEL as previously described. The DED-maps were calculated by subtracting the structure factors for the dark state from the light state ( $|F_{\text{obs}}^{\text{light}}| - |F_{\text{obs}}^{\text{dark}}|$ ) and using the phases from the dark-state structure. Initial difference electron density maps are displayed in figure 22 at a contour level of  $\sigma = 3.5$  for  $\Delta t_{\text{light}} = 2 \text{ ms} - 200 \mu\text{J}$  and  $\Delta t_{\text{light}} = 500 \mu\text{s} - 100 \mu\text{J}$ .

### 9.2 Initial results from pump-probe data collection

In the difference electron density map at  $\Delta t_{\text{light}} = 2 \text{ ms} - 200 \mu\text{J}$  seen in figure 22, we observe a weak negative peak between CO and Fe<sub>a3</sub> and a

weak positive peak between CO and Cu<sub>B</sub>, which indicate a change of CO-ligation from Fe<sub>a3</sub> to Cu<sub>B</sub>. The processing of this data is still on-going and it is likely that the occupancy of the light-activated state is rather low. One could speculate that the initial observations are in line with previous statements of CO-movements occurring after photo-dissociation. It is argued from crystallographic studies on *ba*<sub>3</sub>-type CcO and bovine CcO that CO dislodges from Fe<sub>a3</sub> to Cu<sub>B</sub> upon irradiation [44, 123], although the accuracy of the interpretations from some of these studies can be discussed (see paper IV). Further details on CO-dynamics upon pump irradiation are described in published work where flash-photolysis- and FTIR-studies are performed [129, 134-136], showing CO movement from Fe<sub>a3</sub> to Cu<sub>B</sub> after photo-dissociation.

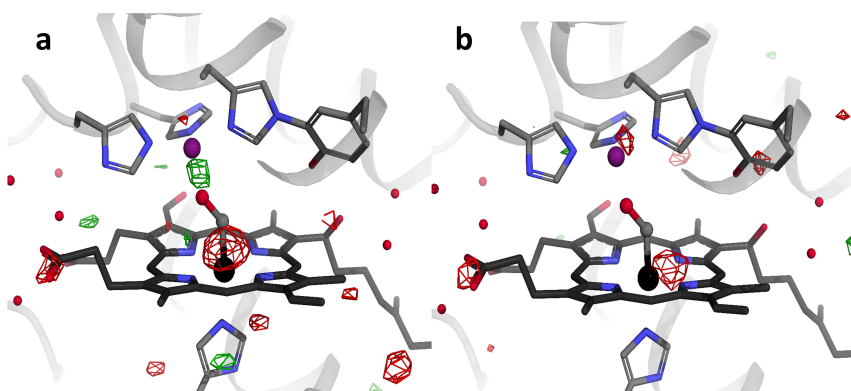


**Figure 22.** The active site of *ba*<sub>3</sub>-type CcO with difference electron density maps contoured at  $\sigma=3.5$  with positive (green) and negative (red) densities at time points (a) 2 ms after pump-laser irradiation at 200  $\mu\text{J}$  and (b) 500  $\mu\text{s}$  after pump laser irradiation at 100  $\mu\text{J}$ .

### 9.3 Discussion and future prospects

The efficiency of reaction triggering in a pump-probe setup is influenced by laser power, crystal size, the scattering properties of the medium and whether the laser traverses the medium before it hits a crystal (crystal position relative to the pump laser interaction region). Sufficient laser power is essential in order to produce an abundant occupancy of the photolysed state. In the study of Kubo et al., an open setup (not including a helium chamber) was used which allowed for laser pumping from two different directions [124]. This set-up was also used for recording the time-resolved “3D-movie” of bR by LCP-SFX [75]. Too high laser power can compromise diffraction quality of the crystals or induce biologically

irrelevant structural changes, due to heating. In solution scattering experiments, laser power titrations are performed to test the minimum power corresponding to structural movements, and do not generate excess solvent heating of the sample environment. In the pump-probe experiment described here, it was not possible to conduct a full laser power titration of the protein in LCP media. Instead, it was necessary to rely on calculations and previous experience.

For future experiments, it would be valuable to perform on-line absorption spectroscopy of the LCP-crystals in order to follow the CO-bound state of CcO. This would be valuable to control for successful CO-dislodging from the Fe<sub>a3</sub>-site and to observe CO-diffusion rates in LCP-media. We previously collected pump-probe data on *ba*<sub>3</sub>-type CcO by time-resolved X-ray solution scattering, which indicated structural transitions at  $\Delta t_{\text{light}}=500 \mu\text{s}$  and  $\Delta t_{\text{light}}=2 \text{ms}$  after laser pumping. These results are outside the scope of this thesis and are only mentioned as a teaser for future pump-probe SFX experiments of *ba*<sub>3</sub>-type CcO.

## 10. Conclusions and future perspectives

This thesis has contributed with structural insight on the *ba*<sub>3</sub>-type cytochrome *c* oxidase from the thermophilic bacterium *Thermus thermophilus*. The presented structures of CcO derive from serial femtosecond crystallography diffraction data collected at the SPring-8 Angstrom Compact free electron Laser (SACLA) and are utilized for structural analysis of the oxidized resting state and reduced CO-bound state of *ba*<sub>3</sub>-type CcO in lipidic cubic phase, presented in paper I and IV. In paper I, the first room-temperature structure of CcO is presented which is free from X-ray induced radiation damage, thus representing a more biologically relevant state. We propose that the active site ligand of *ba*<sub>3</sub>-type CcO is a single oxygen species, as opposed to many of the previously solved structures of CcO. In paper II, we present a refined a crystallization procedure that was used for previous work, and present a feasible way to screen, produce and collect large batches of microcrystals in LCP. This well-based microcrystallization in lipidic cubic phase can conveniently be monitored in real-time. The limitations of producing large amounts of well-diffracting crystals in LCP are overcome by this method, and we show proof of concept by presenting novel crystallization conditions for *ba*<sub>3</sub>-type CcO, a bacterial reaction centre (RC<sub>V<sub>ir</sub></sub>) and sensory rhodopsin II. XFELs are currently being commissioned and upgraded around the world and a new era of structural biology is emerging where serial femtosecond crystallography is becoming the ultimate way of studying time-resolved structural changes in proteins at an atomic scale. With the well-based LCP crystallization method as starting point, an SFX- structure of RC<sub>V<sub>ir</sub></sub> with high ubiquinone occupancy could be determined which is presented in paper III, setting the groundwork for studying electron transfers at the millisecond- and sub-picosend time scales. A further development of the well-based crystallization procedure included anaerobic preparation and injection of reduced CO-bound microcrystals of CcO, which lead to the first SFX-structure of CO-bound *ba*<sub>3</sub>-type cytochrome *c* oxidase (paper IV). We have compared our SFX-structure of CO-bound CcO to structures in oxidized and reduced states. We see no structural differences that could be linked to the proton pumping function as seen for the *aa*<sub>3</sub>-type CcO, for which there is a clear conformational transition between the CO-bound and reduced states. These findings suggest that transitions of structural motifs that play key roles for proton pumping in *ba*<sub>3</sub>-type CcO are not resolved by static structures of different redox- or ligand-bound states, but need to be captured by time-resolved structural studies. By the pump-probe approach, carbon monoxide can be dislodged from the active site of

CcO and mimic the conformational changes that follows oxygen binding. With the work in this thesis, we hope to have planted viable seeds for future time-resolved studies of CcO and other membrane proteins by lipidic cubic phase serial microcrystallography.



#### IV. POPULÄRVETENSKAPLIG SAMMANFATTNING

I denna avhandling beskrivs nya metoder inom proteinkristallografi som applicerats för att studera ett protein som kallas cytokrom *c* oxidas (CcO). Ungefär 90% av syret vi andas används upp av CcO – det är ett protein som är en essentiell del av cellens energiutvinnande system och är en del av "cellens kraftverk" efter att energirik föda brutits ner och förädlats till energirika elektroner. Energirika elektroner kommer träder in i "cellens kraftverk" som kallas mitokondrien, och överförs till olika proteinkomplex som sitter i cellmembranet eller "höljet" av mitokondrien. Elektronerna överförs då till en kedja av olika proteiner som utgör elektrontransportkedjan. Då elektronerna överförs mellan proteinerna i kedjan frigörs energi, som används till att pumpa protoner över cellmembranet. Den sista elektron-acceptorn i kedjan är CcO som är slutstationen, där elektronerna doneras till syret vi andas. I denna process omvandlas ett syre till två vattenmolekyler. Samtidigt som denna omvandling äger rum, frigörs energi som används till att pumpa protoner över cellmembranet, vilket bidrar till att generera en potentiell energi, eller en spänning, över mitokondriens membran (alltså det inre och yttre höljet), som sedan används till att producera ATP, som är kroppens transporterbara energimolekyl. Vi vet ännu inte i dagsläget vilka strukturella förändringar som sker då CcO pumpar protoner över membranet; det enda vi med säkerhet vet är att det är en process som inte kan ske utan elektronöverföringen till syre. I denna avhandling har en klass av CcO studerats som kommer från den termofila bakterien *Thermus Thermophilus*, *ba*<sub>3</sub>-klassen av CcO, som pumpar protoner enbart via en kanal, till skillnad från våra celler där CcO använder två eller tre kanaler för att pumpa protoner. Hädanefter hänvisas det till *ba*<sub>3</sub>-typ CcO.

Ett sätt att förstå proteiners funktion och mekanismer är genom att titta på hur dessa är uppbyggda och kartlägga funktionen av de olika delarna. Inom strukturbologi används metoder som kristallografi och seriekristallografi för att i atomär upplösning titta på hur varje atom i ett protein sitter, i 3D. Avstånden mellan atomerna i proteiner är i skalan  $10^{-10}$  m, och det finns inga mikroskop som kan återge denna upplösning. Därför används röntgenstrålar, som har omkring samma våglängd, för att urskilja atomerna i proteiner. Proteinkristaller innehåller tusentals ordnade atomer, som sitter i regelbundna och repetitiva mönster. Då röntgenstrålar träffar flera liknande atomer och reflekteras, likt vanligt ljus som bryts, förstärks intensiteten i den reflekterade röntgenstrålarna och förstärker signalen.

Med hjälp av matematiska funktioner kan man sedan omvandla dessa reflektioner till 3D-strukturer av proteiner, atom för atom.

Vi har utvecklat en metod för produktion av mikrokristaller av proteiner i lipidisk kubisk fas (LCP). Den lipidiska fasen liknar proteinernas naturliga miljö i cellmembranet, som består av lipider (fett). Metoden som utvecklats kan användas för att effektivt producera och hitta olika kemiska förhållanden för mikrokristaller i LCP, i mängder som inte varit möjliga förut. Denna metod baseras på att kristallisera i brunnar istället för sprutor, vilket också gör det lätt att följa kristalliseringsprocessen från ett mikroskop. Denna metod har möjliggjort strukturbestämningen av CcO i oxiderat "naturligt" stadiet och i reducerat kolmonoxidbundet stadiet. Datat för dessa strukturer samlades under biologiskt relevanta förhållanden (i rumstemperatur) och kristallerna utsattes inte för strålningsrelaterade skador, vilket potentiellt kan skada kvalitén av diffraktions-datat. Den utvecklade metoden har också använts för att kristallisera membranproteinerna Reaction Center och Sensory Rhodopsin II.

Ett sätt att studera proteiners mekanism är genom att titta på hur strukturen hos dem förändras i realtid, då t.ex. ett substrat tillsätts eller då en molekyl binder in till proteinet. Gällande CcO, är det intressant att titta på när kolmonoxid binder in, eftersom kolmonoxid hämmar syrets inbindning, utan att starta irreversibla reaktioner. Dessa reaktioner kan studeras med tidsupplöst proteinkristallografi på XFEL-faciliteter, som har mycket fotontäta röntgenstrålar med hög frekvens och korta pulser. En ström av mikrokristaller skickas genom punkten där röntgenstrålen träffar, och via en laser eller andra metoder (som t.ex. värme eller pH-förändring) kan en reaktion triggas igång som får proteinet att "jobba" och ändra struktur, vilket i sin tur fångas med en ögonblicksbild av röntgenstrålen. Då dessa XFEL-strålar är mycket höga på energi, så förstörs mikrokristallerna precis efter att de träffats, men en diffraktionsbild (alltså reflektionerna från träffade atomer) hinner samlas innan kristallerna förstörs av röntgenstrålen. Tidsupplöst proteinkristallografi är det nya heta inom strukturbologi, och mycket talar för att membranproteiners struktur och funktion kommer att studeras med denna metod i fokus i framtiden. Därav har arbetet i denna avhandling bidragit till att vidareutveckla metoder som är anpassade för detta ändamål, och applicerats på CcO och andra proteiner. Pararellt har arbetet bidragit till att öka förståelsen för strukturen och funktionen av *ba<sub>3</sub>*-typ CcO i relation till andra klasser av CcO. Detta arbete kan förhoppningsvis bidra till att öka förståelsen för hur CcO och andra proteiner som är nödvändiga för livet på jorden fungerar.

## V. ACKNOWLEDGEMENTS

The Lundberg Lab has been a great place at work at. It is packed with lovely people that are kind and encouraging, and I have made many life-long friends here. I would really like to thank all of you, both oldies and newbies, for contributing to all that this workplace is!

First of all, I would like to thank you, **Gisela**. Since the day I met you, you have been like a superhero to me! Your intelligence, kindness, passion for science, humor and taste for adventures really inspire me! It has been a pleasure to work with and learn from you, and I am really grateful that you took me under your wings during these years! I think it is great that your group has expanded this last year, and I am really proud to have been a part of it! Thank you **Richard** for being a great co-supervisor and an inspirational person. Your concerns for all Ph.D.-students well-being, has always felt great. Your laughter is contagious and even though I don't always get the references, I still laugh with you! Keep on singing in the corridor! Thank you **Martin** for being my examiner, I have appreciated our ISP-meetings and your perspective on my work!

To the **Brändénians**, you are the best! **Rebecka**, my golden girl, even though you are in Richards group I have always considered you as a part of our group. I wish we had more beamtimes together, because being with you is always so much fun! Thank you for being such a strong force and laying the foundation for the oxidase project. And thank you for all the fun fika-topics and laughter!! **Swagatha**, you are a truly passionate, kind and generous person, thank you for being who you are! I had a great time with you at ebec! **Jonathan**, you are a star, I cheer on you! I can't wait to see how your Ph.D turns out, it was really a pleasure to have you as a student, and I am really happy that you started in Giselas group! **Duuuunge**, söderbröderglöder for sure! X-ravens/ravers will thrive at MAXIV with you in command, find new worthy members to the crew! **Petra E.**, it's goddamn great to have you back! I wish I was more like you, #big-fan-of yours! **Jennie**, soon it is your turn to defend, I was always impressed with your work and I am cheering on you! **Owens** and **Doris**, you provide great energy to the group, keep on laughing! Btw I can't wait to see some of those dance moves of yours some day! **Peter D.**, I always enjoyed to work and travel with you, you are a strong force to the oxidase project, thank you for all the help with the glove box and great support at the beamtimes! **Emil G.**, so nice to have you in the group! You were one of the best

students when I teached, I was really happy when you started your PhD! **Calle**, you seem like the person who has “stenkoll på saker”, I’m confident that caged oxygen will be a success! **Eriko** and **Rie**, words cannot describe how much I enjoyed working with you! Thank you for hosting us in Japan and bringing in so much valuable ideas to the oxidase project! **Peter B.**, it has been really nice to visit your lab in Stockholm! Thank you for letting me learn more about the oxidase mutants! **Fede**, I always had fun working with you and you learned me a lot about flow-flash and flash-photolysis! I hope to see you soon either here or in Stockholm, can’t wait to meet your dogs! **The Neutze group!** Big welcome to **Analia** and **Lucia**, it is so nice to have you around! **Adams**, you are really nice and it is great to have another data analysis person in the lab! **Greger**, the professor! We started at the same time and I’ve always had interesting conversations with you, about everything from movies to running and your love for BALLS! **Giorgia**, you are a rebel! One of the best conversations we had was on a train in Japan, when you shared some stories from your life. Good luck! **Rob B.**, when I finally started to understand British accent, I really appreciated your sarcastic humor! Thanks for all your support and your optimism (and let’s not mention that hotel I picked in Japan...) You will rock on your defense!! **Daniel**, my brother from another mother! I don’t think it is possible to find a warmer person than you, you bring a smile almost every time! Don’t lose that, your cooking skills or your creative soul! **Per**, peddan, pärlan...kärt barn har många namn! I am so happy that I got to know you, you are one of the most honorable persons at Lundberg lab, a true Gryffindor fo sho! I still owe you chips, and we have a 65” TV (Pierre says hello). Please bake more of those cookies.. **Petra**, Båtis, we have been through so much together! Except for being a “rock” in the lab that everyone relies on, you have been *my rock* through tough times. (cheesy I know)... You’ve always had a warm hug or a listening ear, and I couldn’t wish for a better office mate or friend. You are wonderful, thanks for everything that you are! **The Westenhoffs - Sebastian**, thanks for not moving to Uppsala! You have a wonderful group, and I really enjoyed your Kendrick Lamar reference! Welcome to the lab **Lydia** and good luck with your project, hope you like Swedish beer soon! **Amke**, I’ve always enjoyed having fika with you, and your lunch boxes always look amaaazing! **Andrea**, the sharp-dressed man (at least when you haven’t laundered for weeks) ;) You are a really caring person and I wish you the best of luck, don’t work too hard! **Lauras**, you always bring a smile (and smooth face)! Good luck with your studies! **Claire**, it was always nice to chat with you in the hallway, hope to see you soon! **Matt**, you are the coolest guy in the lab! I always find myself saying weird stuff when you

are around, sorry for that! And good luck with everything in the future! **Joachim**, Jo-Jo (not J-Lo) let's hope it doesn't take too long before we go to a metal concert again!! **Weixiao**, Wejjan, I really appreciate your honesty, I especially recall when I was new in the lab and the peristaltic pump was giving me a hard time...thank you!! My own **Elin**, born and raised together i Jönnet! I was soooo happy to join your class at ED and then I was soooooo happy you were here at Lundberg before me! I thank my lucky star for that! Thanks for being a great friend, and for all the crazy fun, I hope our paths in life continue to lead us together (but not for another Ph.D).. **Léo**, je t'adore! Thanks for being one of the most positive and encouraging friends ever, whenever I had trouble on my mind we could talk and it always felt better afterwards. Plus, I have loooooots of fun with you! Bisous! **Michal**, thanks for bringing in such a nice group to Lundberg! **Anne**, you are super nice and fun, and I think you are really talented in Swedish! **Manoop**, good luck with the research!

The downstairs crowd, you are so many now! **Johanna**, you are a real role model I admire the true passion you have for science! You really inspire me! **Davide**, it was always a comfort to chat with you during all those hours in front of the glove box. Your calmness and positivity is something I strive for! **Jake**, **Dimitra** and **Katharina**, best of luck with your studies, from what I hear you are doing really great!

**The Burmanns – Björn**, thank you for being such a positive and nice P.I! **Irena**, it is always nice to chat with you, keep that smile! **Darius**, the ÄKTA prodigy, keep on playing that beach volleyball, I would love to join sometime! **Emelie**, it's so fun talking with you and you're always so energetic!! **Ylber**, you are super fun! Keep on untzing and bringing entertaining topics to the fika table! **Laura**, I love your laughter, it is not possible to be grumpy around you! **Damasus** and **Jens**, good luck with your Ph.D-studies! **Lisa** and **Josh**, I admire the dedication to your work! Thanks for keeping an eye on the lab at all times!

**The Katona group – Gergely**, I enjoyed your clever jokes and I think you are a genius! Good luck with all the work! **Viktor**, you are a truly kind person, and I love the words of wisdom you once said when I was being negative. **Maja** a.k.a Ratsit, I really like the way you “nail” things(!). We shared a lot of laughter together, good luck with everything! **Kristina**, thank you for always bringing a nice atmosphere! **Rasmus** and **Jessica**, best of luck with your studies, keep on running Göteborgsvarvet for me as well! **Flo**, my raving-rocking friend, I am so happy to have shared fun events and music taste with you throughout the years! I always had a great time with you, and you are probably one of the kindest persons on the planet!

**The best Oldies: Oskar, Emil, David, Cecilia W, Stephan S., Ash, Stephan N.** - I really miss having you around! You made Lundberg great! **Rhawnie**, when will we go out and dance the TT-moves! Miss u! **Elin D.**, I really miss you here in Gothenburg! I hope life is great in Uppsala! **Dodsy**, it's great to have you back at bästkusten soon, you really left an empty space here! **Linnea**, you're wonderful, I can't stand knowing you're not at Lundberg now! **Majo**, Dr. Mojo, my dear friend, you are such cool and kind person, I really admire you! I can't wait to hang out more here in Gbg and in Spain! **Tinna**, if I would vote for a president that would be you! I always love to be around you! Hope you, me and Majo could dive together sometime! **Bruno**, I always came to you with problems, but left with solutions, you were always there to help me out! I really enjoy our conversations and admire all your knowledge and the work you do! **Valida** and **Lars**, thanks for being the foundation of this lab!

**Mina vänner utanför labbet: ni vet vilka ni är!** Ni har hjälp mig igenom dem här 4 åren, tack för att ni alltid finns där och hejar på mig!

**Roger, Wiveka, Douglas, Eveliina, Richard, Mia, Irene och hela härliga släkten** – jag är så glad att ha er som familj! Er kärlek och stöttning värmer bara jag tänker på den, och jag ser så mycket fram emot att ha mer tid att spendera tillsammans med er!

**Mamma, André, Vicki och Simon**, ingenting av det här hade varit möjligt utan ert stöd och all er oändliga kärlek! Ni har funnits där ovillkorligen, dag som natt, och alltid trott på mig! Tack, jag älskar er så mycket!

**Pierre**, du är mitt livs kärlek! Vi har genomgått många prövningar ihop, men ändå står vi starkare än någonsin tillsammans! Du får mig alltid att skratta, du lär mig massor om allt och livet är så underbart med dig! Allt är liksom möjligt! Jag hoppas att jag kan vara ett lika bra stöd för dig i framtiden som du har varit för mig, och jag längtar efter varje ny dag ihop med dig! Älskar dig mest!

## VI. BIBLIOGRAPHY

1. Johnson, M.P., *Photosynthesis*. Essays in biochemistry, 2016. **60**(3): p. 255-273.
2. Mitchell, P., *Chemiosmotic coupling in oxidative and photosynthetic phosphorylation*. Biochimica et Biophysica Acta (BBA) - Bioenergetics, 2011. **1807**(12): p. 1507-1538.
3. Ramsay, R.R., *Electron carriers and energy conservation in mitochondrial respiration*. ChemTexts, 2019. **5**(2): p. 9.
4. Vinogradov, A.D., *Steady-state and pre-steady-state kinetics of the mitochondrial F(1)F(o) ATPase: is ATP synthase a reversible molecular machine?* Journal of Experimental Biology, 2000. **203**(1): p. 41.
5. Yang, S.-H. and R. Liu, *For the pursuit of oxygen and carbon dioxide channels in mitochondria*. Medical gas research, 2016. **6**(4): p. 237-238.
6. Wikström, M., K. Krab, and V. Sharma, *Oxygen Activation and Energy Conservation by Cytochrome c Oxidase*. Chemical reviews, 2018. **118**(5): p. 2469-2490.
7. García-Horsman, J.A., et al., *The superfamily of heme-copper respiratory oxidases*. Journal of Bacteriology, 1994. **176**(18): p. 5587.
8. Shapleigh, J.P., et al., *Definition of the catalytic site of cytochrome c oxidase: specific ligands of heme a and the heme a<sub>3</sub>-Cu<sub>B</sub> center*. Proc Natl Acad Sci U S A, 1992. **89**(11): p. 4786-90.
9. Pereira, M.M., M. Santana, and M. Teixeira, *A novel scenario for the evolution of haem-copper oxygen reductases*. Biochimica et Biophysica Acta (BBA) - Bioenergetics, 2001. **1505**(2): p. 185-208.
10. Wikstrom, M., K. Krab, and V. Sharma, *Oxygen Activation and Energy Conservation by Cytochrome c Oxidase*. Chem Rev, 2018. **118**(5): p. 2469-2490.
11. Iwata, S., et al., *Structure at 2.8 Å resolution of cytochrome c oxidase from Paracoccus denitrificans*. Nature, 1995. **376**(6542): p. 660-669.
12. Tsukihara, T., et al., *The whole structure of the 13-subunit oxidized cytochrome c oxidase at 2.8 Å*. Science, 1996. **272**(5265): p. 1136-44.
13. Soulimane, T., et al., *Structure and mechanism of the aberrant ba(3)-cytochrome c oxidase from thermus thermophilus*. The EMBO journal, 2000. **19**(8): p. 1766-1776.
14. Svensson-Ek, M., et al., *The X-ray Crystal Structures of Wild-type and EQ(I-286) Mutant Cytochrome c Oxidases from Rhodobacter*

- sphaeroides*. Journal of Molecular Biology, 2002. **321**(2): p. 329-339.
15. Schmidt, B., J. McCracken, and S. Ferguson-Miller, *A discrete water exit pathway in the membrane protein cytochrome c oxidase*. Proceedings of the National Academy of Sciences of the United States of America, 2003. **100**(26): p. 15539-15542.
  16. Yano, N., et al., *The Mg<sup>2+</sup>-containing Water Cluster of Mammalian Cytochrome c Oxidase Collects Four Pumping Proton Equivalents in Each Catalytic Cycle*. J Biol Chem, 2016. **291**(46): p. 23882-23894.
  17. Hosler, J.P., *The influence of subunit III of cytochrome c oxidase on the D pathway, the proton exit pathway and mechanism-based inactivation in subunit I*. Biochimica et Biophysica Acta (BBA) - Bioenergetics, 2004. **1655**: p. 332-339.
  18. Gennis, R.B., *Multiple proton-conducting pathways in cytochrome oxidase and a proposed role for the active-site tyrosine*. Biochimica et Biophysica Acta (BBA) - Bioenergetics, 1998. **1365**(1): p. 241-248.
  19. Verkhovskiy, M.I., et al., *Proton translocation by cytochrome c oxidase*. Nature, 1999. **400**(6743): p. 480-3.
  20. Branden, G., R.B. Gennis, and P. Brzezinski, *Transmembrane proton translocation by cytochrome c oxidase*. Biochim Biophys Acta, 2006. **1757**(8): p. 1052-63.
  21. Yoshikawa, S., et al., *Redox-Coupled Crystal Structural Changes in Bovine Heart Cytochrome c Oxidase*. Science, 1998. **280**(5370): p. 1723.
  22. Tomson, F.L., et al., *Substitutions for glutamate 101 in subunit II of cytochrome c oxidase from Rhodobacter sphaeroides result in blocking the proton-conducting K-channel*. Biochemistry, 2003. **42**(6): p. 1711-7.
  23. Kannt, A., et al., *Electrical current generation and proton pumping catalyzed by the ba<sub>3</sub>-type cytochrome c oxidase from Thermus thermophilus*. FEBS Lett, 1998. **434**(1-2): p. 17-22.
  24. Rich, P.R. and A. Maréchal, *Functions of the hydrophilic channels in protonmotive cytochrome c oxidase*. Journal of the Royal Society, Interface, 2013. **10**(86): p. 20130183-20130183.
  25. Lee, H.M., et al., *Mutations in the putative H-channel in the cytochrome c oxidase from Rhodobacter sphaeroides show that this channel is not important for proton conduction but reveal modulation of the properties of heme a*. Biochemistry, 2000. **39**(11): p. 2989-96.
  26. Sharma, V., et al., *Insights into functions of the H channel of cytochrome c oxidase from atomistic molecular dynamics*

- simulations*. Proceedings of the National Academy of Sciences of the United States of America, 2017. **114**(48): p. E10339-E10348.
27. Malkamäki, A., et al., *The H channel is not a proton transfer path in yeast cytochrome c oxidase*. Biochimica et Biophysica Acta (BBA) - Bioenergetics, 2019. **1860**(9): p. 717-723.
  28. Shimokata, K., et al., *The proton pumping pathway of bovine heart cytochrome c oxidase*. Proceedings of the National Academy of Sciences of the United States of America, 2007. **104**(10): p. 4200-4205.
  29. Stuchebrukhov, A.A., *Long-distance electron tunneling in proteins: A new challenge for time-resolved spectroscopy*. Laser Physics, 2010. **20**(1): p. 125-138.
  30. Sazanov, L.A., *A giant molecular proton pump: structure and mechanism of respiratory complex I*. Nature Reviews Molecular Cell Biology, 2015. **16**: p. 375.
  31. Mitchell, P., *The protonmotive Q cycle: a general formulation*. FEBS Lett, 1975. **59**(2): p. 137-9.
  32. Wikstrom, M.K.F., *Proton pump coupled to cytochrome c oxidase in mitochondria*. Nature, 1977. **266**(5599): p. 271-273.
  33. Brzezinski, P., *Redox-driven membrane-bound proton pumps*. Trends in Biochemical Sciences, 2004. **29**(7): p. 380-387.
  34. Mills, D.A. and S. Ferguson-Miller, *Understanding the mechanism of proton movement linked to oxygen reduction in cytochrome c oxidase: lessons from other proteins*. FEBS Lett, 2003. **545**(1): p. 47-51.
  35. Oliveira, A.S.F., et al., *Exploring O<sub>2</sub> Diffusion in A-Type Cytochrome c Oxidases: Molecular Dynamics Simulations Uncover Two Alternative Channels towards the Binuclear Site*. PLOS Computational Biology, 2014. **10**(12): p. e1004010.
  36. Funatogawa, C., et al., *Role of the Conserved Valine 236 in Access of Ligands to the Active Site of Thermus thermophilus ba3 Cytochrome Oxidase*. Biochemistry, 2017. **56**(1): p. 107-119.
  37. Carpenter, E.P., et al., *Overcoming the challenges of membrane protein crystallography*. Current opinion in structural biology, 2008. **18**(5): p. 581-586.
  38. Radzi Noor, M. and T. Soulimane, *Bioenergetics at extreme temperature: Thermus thermophilus ba3- and caa3-type cytochrome c oxidases*. Biochimica et Biophysica Acta (BBA) - Bioenergetics, 2012. **1817**(4): p. 638-649.
  39. Chen, Y., et al., *A homologous expression system for obtaining engineered cytochrome ba3 from Thermus thermophilus HB8*. Protein Expr Purif, 2005. **40**(2): p. 299-318.
  40. Keightley, J.A., et al., *Molecular Genetic and Protein Chemical Characterization of the Cytochrome ba3 from Thermus*

- thermophilus* HB8. Journal of Biological Chemistry, 1995. **270**(35): p. 20345-20358.
41. Seddon, A.M., P. Curnow, and P.J. Booth, *Membrane proteins, lipids and detergents: not just a soap opera*. Biochimica et Biophysica Acta (BBA) - Biomembranes, 2004. **1666**(1): p. 105-117.
  42. Pastorino, L., et al., *Multilayered polyelectrolyte microcapsules: interaction with the enzyme cytochrome C oxidase*. PloS one, 2014. **9**(11): p. e112192-e112192.
  43. Farver, O., et al., *Electron transfer among the CuA-, heme b- and a<sub>3</sub>-centers of Thermus thermophilus cytochrome ba<sub>3</sub>*. FEBS Letters, 2006. **580**(14): p. 3417-3421.
  44. Liu, B., et al., *Structural changes that occur upon photolysis of the Fe(II)(a<sub>3</sub>)-CO complex in the cytochrome ba(3)-oxidase of Thermus thermophilus: a combined X-ray crystallographic and infrared spectral study demonstrates CO binding to Cu(B)*. Biochim Biophys Acta, 2012. **1817**(4): p. 658-65.
  45. Fabian, M. and B. Malmström, *The effect of pH changes on the optical spectrum of oxidised cytochrome oxidase*. Biochimica et Biophysica Acta (BBA) - Bioenergetics, 1989. **973**(3): p. 414-419.
  46. Kendrew, J.C., et al., *A three-dimensional model of the myoglobin molecule obtained by x-ray analysis*. Nature, 1958. **181**(4610): p. 662-6.
  47. Deisenhofer, J., et al., *Structure of the protein subunits in the photosynthetic reaction centre of Rhodospseudomonas viridis at 3Å resolution*. Nature, 1985. **318**(6047): p. 618-24.
  48. Campos-Acevedo, A.A., et al., *First attempts to crystallize a non-homogeneous sample of thioredoxin from Litopenaeus vannamei: What to do when you have diffraction data of a protein that is not the target?* Biochemistry and Biophysics Reports, 2016. **8**: p. 284-289.
  49. Russo Krauss, I., et al., *An overview of biological macromolecule crystallization*. Int J Mol Sci, 2013. **14**(6): p. 11643-91.
  50. Caffrey, M. and V. Cherezov, *Crystallizing membrane proteins using lipidic mesophases*. Nature protocols, 2009. **4**(5): p. 706-731.
  51. McPherson, A. and J.A. Gavira, *Introduction to protein crystallization*. Acta crystallographica. Section F, Structural biology communications, 2014. **70**(Pt 1): p. 2-20.
  52. Caffrey, M., *Crystallizing Membrane Proteins for Structure Determination: Use of Lipidic Mesophases*. Annual Review of Biophysics, 2009. **38**(1): p. 29-51.

53. Ostermeier, C. and H. Michel, *Crystallization of membrane proteins*. Current Opinion in Structural Biology, 1997. 7(5): p. 697-701.
54. Ostermeier, C., et al., *Structure at 2.7 Å resolution of the Paracoccus denitrificans two-subunit cytochrome c oxidase complexed with an antibody Fv fragment*. Proceedings of the National Academy of Sciences of the United States of America, 1997. 94(20): p. 10547-10553.
55. Ostermeier, C., et al., *Fv fragment-mediated crystallization of the membrane protein bacterial cytochrome c oxidase*. Nature Structural Biology, 1995. 2(10): p. 842-846.
56. Ujwal, R. and J.U. Bowie, *Crystallizing membrane proteins using lipidic bicelles*. Methods (San Diego, Calif.), 2011. 55(4): p. 337-341.
57. Faham, S. and J.U. Bowie, *Bicelle crystallization: a new method for crystallizing membrane proteins yields a monomeric bacteriorhodopsin structure* Edited by D. Rees. Journal of Molecular Biology, 2002. 316(1): p. 1-6.
58. Cherezov, V., *Lipidic Cubic Phase Technologies for Membrane Protein Structural Studies*. Current opinion in structural biology, 2011. 21(4): p. 559-566.
59. Kulkarni, C.V., et al., *Monoolein: a magic lipid?* Phys Chem Chem Phys, 2011. 13(8): p. 3004-21.
60. Caffrey, M., *A comprehensive review of the lipid cubic phase or in meso method for crystallizing membrane and soluble proteins and complexes*. Acta Crystallogr F Struct Biol Commun, 2015. 71(Pt 1): p. 3-18.
61. Zabara, A., et al., *Lipidic Cubic Phase-Induced Membrane Protein Crystallization: Interplay Between Lipid Molecular Structure, Mesophase Structure and Properties, and Crystallogenesis*. Crystal Growth & Design, 2017. 17(11): p. 5667-5674.
62. Caffrey, M., et al., *'Hit and run' serial femtosecond crystallography of a membrane kinase in the lipid cubic phase*. Philos Trans R Soc Lond B Biol Sci, 2014. 369(1647): p. 20130621.
63. Maddox, B., *The double helix and the 'wronged heroine'*. Nature, 2003. 421(6921): p. 407-408.
64. Patel, N., *Shorter, brighter, better*. Nature, 2002. 415(6868): p. 110-111.
65. Diederichs, K. and M. Wang, *Serial Synchrotron X-Ray Crystallography (SSX)*, in *Protein Crystallography: Methods and Protocols*, A. Wlodawer, Z. Dauter, and M. Jaskolski, Editors. 2017, Springer New York: New York, NY. p. 239-272.

66. Pflugrath, J.W., *Practical macromolecular cryocrystallography*. Acta crystallographica. Section F, Structural biology communications, 2015. **71**(Pt 6): p. 622-642.
67. Ebrahim, A., et al., *Dose-resolved serial synchrotron and XFEL structures of radiation-sensitive metalloproteins*. IUCrJ, 2019. **6**(4): p. 543-551.
68. Neutze, R., et al., *Potential for biomolecular imaging with femtosecond X-ray pulses*. Nature, 2000. **406**(6797): p. 752-757.
69. Cusack, S., et al., *Small is beautiful: protein microcrystallography*. Nature Structural Biology, 1998. **5**: p. 634.
70. Weierstall, U., et al., *Lipidic cubic phase injector facilitates membrane protein serial femtosecond crystallography*. Nature Communications, 2014. **5**: p. 3309.
71. Nam, K.H., *Sample Delivery Media for Serial Crystallography*. Int J Mol Sci, 2019. **20**(5).
72. Hunter, M.S., et al., *Fixed-target protein serial microcrystallography with an x-ray free electron laser*. Scientific Reports, 2014. **4**: p. 6026.
73. Mafune, F., et al., *Microcrystal delivery by pulsed liquid droplet for serial femtosecond crystallography*. Acta Crystallogr D Struct Biol, 2016. **72**(Pt 4): p. 520-3.
74. Sierra, R.G., et al., *Nanoflow electrospinning serial femtosecond crystallography*. Acta crystallographica. Section D, Biological crystallography, 2012. **68**(Pt 11): p. 1584-1587.
75. Nango, E., et al., *A three-dimensional movie of structural changes in bacteriorhodopsin*. Science, 2016. **354**(6319): p. 1552.
76. Sugahara, M., et al., *Grease matrix as a versatile carrier of proteins for serial crystallography*. Nature Methods, 2014. **12**: p. 61.
77. Tono, K., et al., *Diverse application platform for hard X-ray diffraction in SACLA (DAPHNIS): application to serial protein crystallography using an X-ray free-electron laser*. Journal of Synchrotron Radiation, 2015. **22**(3): p. 532-537.
78. Grunbein, M.L. and G. Nass Kovacs, *Sample delivery for serial crystallography at free-electron lasers and synchrotrons*. Acta Crystallographica Section D, 2019. **75**(2): p. 178-191.
79. Hatsui, T. and H. Graafsma, *X-ray imaging detectors for synchrotron and XFEL sources*. IUCrJ, 2015. **2**(3): p. 371-383.
80. Kameshima, T., et al., *Development of an X-ray pixel detector with multi-port charge-coupled device for X-ray free-electron laser experiments*. Review of Scientific Instruments, 2014. **85**(3): p. 033110.

81. Olmos, J.L., et al., *Enzyme intermediates captured “on the fly” by mix-and-inject serial crystallography*. BMC Biology, 2018. **16**(1): p. 59.
82. Stagno, J.R., et al., *Structures of riboswitch RNA reaction states by mix-and-inject XFEL serial crystallography*. Nature, 2016. **541**: p. 242.
83. Ishigami, I., et al., *Snapshot of an oxygen intermediate in the catalytic reaction of cytochrome c oxidase*. Proc Natl Acad Sci U S A, 2019. **116**(9): p. 3572-3577.
84. Moffat, K., *Time-resolved crystallography and protein design: signalling photoreceptors and optogenetics*. Philosophical Transactions of the Royal Society B: Biological Sciences, 2014. **369**(1647): p. 20130568.
85. Sanchez-Gonzalez, A., et al., *Coincidence timing of femtosecond optical pulses in an X-ray free electron laser*. Journal of Applied Physics, 2017. **122**(20): p. 203105.
86. Suga, M., et al., *Light-induced structural changes and the site of O=O bond formation in PSII caught by XFEL*. Nature, 2017. **543**: p. 131.
87. Shimada, A., et al., *A nanosecond time-resolved XFEL analysis of structural changes associated with CO release from cytochrome c oxidase*. Sci Adv, 2017. **3**(7): p. e1603042.
88. Pande, K., et al., *Femtosecond structural dynamics drives the trans/cis isomerization in photoactive yellow protein*. Science, 2016. **352**(6286): p. 725-9.
89. Tosha, T., et al., *Capturing an initial intermediate during the P450<sub>nor</sub> enzymatic reaction using time-resolved XFEL crystallography and caged-substrate*. Nature Communications, 2017. **8**(1): p. 1585.
90. Kirian, R.A., et al., *Femtosecond protein nanocrystallography—data analysis methods*. Optics Express, 2010. **18**(6): p. 5713-5723.
91. Beyerlein, K.R., et al., *FELIX: an algorithm for indexing multiple crystallites in X-ray free-electron laser snapshot diffraction images*. Journal of applied crystallography, 2017. **50**(Pt 4): p. 1075-1083.
92. Nakane, T., et al., *Data processing pipeline for serial femtosecond crystallography at SACLA*. Journal of applied crystallography, 2016. **49**(Pt 3): p. 1035-1041.
93. Barty, A., et al., *Cheetah: software for high-throughput reduction and analysis of serial femtosecond X-ray diffraction data*. Journal of Applied Crystallography, 2014. **47**(3): p. 1118-1131.

94. White, T.A., et al., *CrystFEL: a software suite for snapshot serial crystallography*. Journal of Applied Crystallography, 2012. **45**(2): p. 335-341.
95. Karplus, P.A. and K. Diederichs, *Assessing and maximizing data quality in macromolecular crystallography*. Current opinion in structural biology, 2015. **34**: p. 60-68.
96. Karplus, P.A. and K. Diederichs, *Linking crystallographic model and data quality*. Science (New York, N.Y.), 2012. **336**(6084): p. 1030-1033.
97. *The CCP4 suite: programs for protein crystallography*. Acta Crystallogr D Biol Crystallogr, 1994. **50**(Pt 5): p. 760-3.
98. Emsley, P. and K. Cowtan, *Coot: model-building tools for molecular graphics*. Acta Crystallographica Section D, 2004. **60**(12 Part 1): p. 2126-2132.
99. Murshudov, G.N., et al., *REFMAC5 for the refinement of macromolecular crystal structures*. Acta crystallographica. Section D, Biological crystallography, 2011. **67**(Pt 4): p. 355-367.
100. Au - Li, D., et al., *Use of a Robot for High-throughput Crystallization of Membrane Proteins in Lipidic Mesophases*. JoVE, 2012(67): p. e4000.
101. Gaisford, W., G. Schertler, and P. Edwards, *mosquito® LCP: Making membrane protein crystallization accessible to the research scientist*. Nature Methods, 2011. **8**: p. 520.
102. Liu, W., A. Ishchenko, and V. Cherezov, *Preparation of microcrystals in lipidic cubic phase for serial femtosecond crystallography*. Nature protocols, 2014. **9**(9): p. 2123-2134.
103. Wacker, D., et al., *Structural features for functional selectivity at serotonin receptors*. Science, 2013. **340**(6132): p. 615-9.
104. Cherezov, V. and M. Caffrey, *Nano-volume plates with excellent optical properties for fast, inexpensive crystallization screening of membrane proteins*. Journal of Applied Crystallography, 2003. **36**(6): p. 1372-1377.
105. Liu, W., A. Ishchenko, and V. Cherezov, *Preparation of microcrystals in lipidic cubic phase for serial femtosecond crystallography*. Nat Protoc, 2014. **9**(9): p. 2123-34.
106. Au - Ishchenko, A., V. Au - Cherezov, and W. Au - Liu, *Preparation and Delivery of Protein Microcrystals in Lipidic Cubic Phase for Serial Femtosecond Crystallography*. JoVE, 2016(115): p. e54463.
107. Wadsten, P., et al., *Lipidic Sponge Phase Crystallization of Membrane Proteins*. Journal of Molecular Biology, 2006. **364**(1): p. 44-53.

108. Tiefenbrunn, T., et al., *High resolution structure of the ba3 cytochrome c oxidase from Thermus thermophilus in a lipidic environment*. PLoS One, 2011. **6**(7): p. e22348.
109. McCoy, A.J., et al., *Phaser crystallographic software*. Journal of Applied Crystallography, 2007. **40**(4): p. 658-674.
110. Woelke, A.L., et al., *Proton transfer in the K-channel analog of B-type Cytochrome c oxidase from Thermus thermophilus*. Biophysical journal, 2014. **107**(9): p. 2177-2184.
111. Chang, H.-Y., et al., *The cytochrome ba3 oxygen reductase from Thermus thermophilus uses a single input channel for proton delivery to the active site and for proton pumping*. Proceedings of the National Academy of Sciences of the United States of America, 2009. **106**(38): p. 16169-16173.
112. Hunsicker-Wang, L.M., et al., *A novel cryoprotection scheme for enhancing the diffraction of crystals of recombinant cytochrome ba3 oxidase from Thermus thermophilus*. Acta Crystallogr D Biol Crystallogr, 2005. **61**(Pt 3): p. 340-3.
113. Liu, B., et al., *Combined microspectrophotometric and crystallographic examination of chemically reduced and X-ray radiation-reduced forms of cytochrome ba3 oxidase from Thermus thermophilus: structure of the reduced form of the enzyme*. Biochemistry, 2009. **48**(5): p. 820-6.
114. Liu, B., et al., *An unexpected outcome of surface engineering an integral membrane protein: improved crystallization of cytochrome ba(3) from Thermus thermophilus*. Acta Crystallogr Sect F Struct Biol Cryst Commun, 2007. **63**(Pt 12): p. 1029-34.
115. Luna, V.M., et al., *Mobility of Xe Atoms within the Oxygen Diffusion Channel of Cytochrome ba3 Oxidase*. Biochemistry, 2012. **51**(23): p. 4669-4676.
116. McDonald, W., et al., *Ligand access to the active site in Thermus thermophilus ba(3) and bovine heart aa(3) cytochrome oxidases*. Biochemistry, 2013. **52**(4): p. 640-52.
117. Hirata, K., et al., *Determination of damage-free crystal structure of an X-ray-sensitive protein using an XFEL*. Nat Methods, 2014. **11**(7): p. 734-6.
118. Kaila, V.R., et al., *A combined quantum chemical and crystallographic study on the oxidized binuclear center of cytochrome c oxidase*. Biochim Biophys Acta, 2011. **1807**(7): p. 769-78.
119. von Ballmoos, C., et al., *Mutation of a single residue in the ba3 oxidase specifically impairs protonation of the pump site*. Proc Natl Acad Sci U S A, 2015. **112**(11): p. 3397-402.
120. Paulus, A., et al., *The cytochrome ba3 oxidase from Thermus thermophilus does not generate a tryptophan radical during*

- turnover: Implications for the mechanism of proton pumping. *Biochimica et Biophysica Acta (BBA) - Bioenergetics*, 2015. **1847**(10): p. 1093-1100.
121. Nass, K., et al., *Indications of radiation damage in ferredoxin microcrystals using high-intensity X-FEL beams*. *J Synchrotron Radiat*, 2015. **22**(2): p. 225-38.
122. Nass, K., *Radiation damage in protein crystallography at X-ray free-electron lasers*. *Acta Crystallogr D Struct Biol*, 2019. **75**(Pt 2): p. 211-218.
123. Ishigami, I., et al., *Crystal structure of CO-bound cytochrome c oxidase determined by serial femtosecond X-ray crystallography at room temperature*. *Proceedings of the National Academy of Sciences of the United States of America*, 2017. **114**(30): p. 8011-8016.
124. Kubo, M., et al., *Nanosecond pump-probe device for time-resolved serial femtosecond crystallography developed at SACLA*. *Journal of Synchrotron Radiation*, 2017. **24**(5): p. 1086-1091.
125. Muramoto, K., et al., *Bovine cytochrome c oxidase structures enable O<sub>2</sub> reduction with minimization of reactive oxygens and provide a proton-pumping gate*. *Proc Natl Acad Sci U S A*, 2010. **107**(17): p. 7740-5.
126. Tsukihara, T., et al., *The low-spin heme of cytochrome c oxidase as the driving element of the proton-pumping process*. *Proc Natl Acad Sci U S A*, 2003. **100**(26): p. 15304-9.
127. Qin, L., et al., *Redox-dependent conformational changes in cytochrome C oxidase suggest a gating mechanism for proton uptake*. *Biochemistry*, 2009. **48**(23): p. 5121-5130.
128. Ishigami, I., et al., *Crystal structure of CO-bound cytochrome c oxidase determined by serial femtosecond X-ray crystallography at room temperature*. *Proc Natl Acad Sci U S A*, 2017. **114**(30): p. 8011-8016.
129. Heitbrink, D., et al., *Transient Binding of CO to Cu<sub>B</sub> in Cytochrome c Oxidase Is Dynamically Linked to Structural Changes around a Carboxyl Group: A Time-Resolved Step-Scan Fourier Transform Infrared Investigation*. *Biophysical Journal*, 2002. **82**(1): p. 1-10.
130. Szundi, I., et al., *CO impedes superfast O<sub>2</sub> binding in ba<sub>3</sub> cytochrome oxidase from *Thermus thermophilus**. *Proc Natl Acad Sci U S A*, 2010. **107**(49): p. 21010-5.
131. Schäfer, J., et al., *Regulation of cytochrome c oxidase activity by modulation of the catalytic site*. *Scientific Reports*, 2018. **8**(1): p. 11397.

132. Brzezinski, P. and B.G. Malmstrom, *The reduction of cytochrome c oxidase by carbon monoxide*. FEBS Lett, 1985. **187**(1): p. 111-4.
133. Nogly, P., et al., *Lipidic cubic phase injector is a viable crystal delivery system for time-resolved serial crystallography*. Nature Communications, 2016. **7**(1): p. 12314.
134. Koutsoupakis, C., T. Soulimane, and C. Varotsis, *Spectroscopic and kinetic investigation of the fully reduced and mixed valence states of ba3-cytochrome c oxidase from Thermus thermophilus: a Fourier transform infrared (FTIR) and time-resolved step-scan FTIR study*. J Biol Chem, 2012. **287**(44): p. 37495-507.
135. Einarsdottir, O., et al., *Photodissociation and recombination of carbonmonoxy cytochrome oxidase: Dynamics from picoseconds to kiloseconds*. Biochemistry, 1993. **32**(45): p. 12013-12024.
136. Hill, B.C., *The pathway of CO binding to cytochrome c oxidase. Can the gateway be closed?* FEBS Lett, 1994. **354**(3): p. 284-8.